

**DENSITY OF STATES  
CALCULATIONS FOR CARBON  
ALLOTROPES AND MIXTURES**

**EDUARDO WARSZAWSKI**



# DENSITY OF STATES CALCULATIONS FOR CARBON ALLOTROPES AND MIXTURES

Research Thesis

Submitted in Partial Fulfillment of the Requirements

For the Degree of Master of Science

in Physics

**EDUARDO WARSZAWSKI**

Submitted to the Senate of the Technion — Israel Institute of Technology

TEBETH 5769

HAIFA

DECEMBER 2008



The Research Thesis Was Done Under The Supervision of Dr. Joan Adler and Prof.  
Alon Hoffman in The DEPARTMENT OF PHYSICS

## Acknowledgment

I wish to express my gratitude to Dr. J. Adler and Prof. A. Hoffman for the guidance, support and understanding during this research.

The generous financial help of THE TECHNION is gratefully acknowledged



# Contents

<b>Abstract</b>	<b>xv</b>
<b>1 Introduction</b>	<b>1</b>
1.1 Carbon allotropes . . . . .	1
1.2 Diamond . . . . .	4
1.3 Graphite . . . . .	5
1.4 Graphene . . . . .	7
1.5 Amorphous structures . . . . .	7
1.6 Objectives . . . . .	9
<b>2 Experimental techniques</b>	<b>11</b>
2.1 NEXAFS . . . . .	11
2.1.1 Theory . . . . .	13
2.2 Diamond nucleation with hydrogen . . . . .	15
<b>3 Simulation Techniques</b>	<b>19</b>
3.1 Ab-initio . . . . .	19
3.2 LCAO calculations . . . . .	19
3.3 Molecular dynamics . . . . .	22

3.3.1	Semi-empirical potentials . . . . .	22
3.3.2	Tight binding molecular dynamics . . . . .	23
3.3.3	The tight-binding model . . . . .	24
3.3.4	Energy calculations . . . . .	27
3.3.5	Rescaling functions . . . . .	28
3.3.6	Simulation steps . . . . .	29
3.4	Annealing and quenching . . . . .	30
3.5	Density of states . . . . .	32
3.6	k-sampling . . . . .	33
3.7	Coordination number . . . . .	34
3.8	Periodic boundary conditions . . . . .	35
3.9	Visualization . . . . .	36
3.10	Plato . . . . .	36
<b>4</b>	<b>Sample characterization and preparation</b>	<b>39</b>
4.1	Recharacterization . . . . .	39
4.2	Cutting the sample . . . . .	41
<b>5</b>	<b>Results</b>	<b>43</b>
5.1	Calibration samples . . . . .	43
5.1.1	DOS, LDOS and RDF calculation in different regular samples	43
5.1.2	Diamond . . . . .	44
5.1.3	Vacancy DOS comparison . . . . .	47
5.1.4	Graphite and graphene . . . . .	49
5.2	Amorphous carbon . . . . .	50
5.2.1	Amorphous carbon in the entire sample . . . . .	52



5.3	Mixed samples . . . . .	59
5.3.1	Making an amorphous nucleus in diamond crystals . . . . .	59
5.3.2	DOS comparisons . . . . .	60
5.4	Hydrogen in diamond . . . . .	64
<b>6</b>	<b>Discussion and summary</b>	<b>67</b>
<b>A</b>	<b>Programming techniques</b>	<b>69</b>
	<b>References</b>	<b>76</b>
	<b>Hebrew Abstract</b>	<b>v</b>



# List of Figures

1.1	P, T phase diagram of carbon reproduced from [1]. . . . .	2
1.2	Representation of $sp^3$ hybridization . . . . .	4
1.3	Visualization of a diamond lattice. . . . .	5
1.4	Representation of $sp^2$ hybridization . . . . .	6
1.5	Perspective and normal views of a graphite model. Note the interlock of the planes on the right picture. . . . .	7
1.6	One graphene sheet. . . . .	8
1.7	Amorphous carbon model. $sp^2$ bonds are colored in green, $sp^3$ in blue. . . . .	8
2.1	Basic process (left) and composition (right) of the NEXAFS spectra. [2]	12
2.2	NEXAFS fundamental phenomena. [3] . . . . .	13
4.1	A sample of 5120 carbon atoms, in a diamond structure, after damage and after annealing. On the left the complete sample. On the right, a cut at the center where the graphitization process is clearly observed. $sp^3$ atoms are colored in blue, $sp^2$ atoms and bonds are colored in green. The border atoms are painted in brown. . . . .	40

4.2	Two detailed views of the previous sample of 5120 carbon atoms. A cut of the center is shown. The graphitic planes are clearly presented. $sp^3$ atoms are colored in blue, $sp^2$ atoms and bonds are colored in green.	40
4.3	Two views of 6x6x6 unit cell, after damage and after annealing. The graphitic planes are easily appreciated. Compare with Figure 4.4. $sp^3$ atoms are colored in blue, $sp^2$ atoms and bonds are colored in green.	41
4.4	This figure is taken from the original work of Saada et al. [4]. Only threefold coordinated atoms and their nearest neighbors (if threefold) are displayed and connected by bonds. White and black spheres indicate threefold and fourfold coordinated atoms respectively. The graphitic planes are observed at the bottom of the picture.	42
5.1	Orthogonal and Frauenheim DOS comparison.	45
5.2	Special vs Monkhorst-Pack k-point selection.	45
5.3	Variable number of k-points comparison.	46
5.4	DOS scaling variation with the number of atoms.	46
5.5	Detailed comparison between DOS calculation and NEXAFS for CVD diamond.	47
5.6	Graphs of DOS as a function of energy in eV. Upper image: perfect diamond configuration. Lower image: diamond with vacancy. The characteristic <i>blip</i> result of the free states due to the vacancy is observed in the gap at the Fermi energy (red line).	48
5.7	Graphite DOS calculation for 512 C atoms	49
5.8	NEXAFS (arbitrary units) as a function of energy in eV for HOPG. [5]	50
5.9	DOS for a graphene sheet.	51

5.10	Two views of 512 carbon atoms in a perfect diamond configuration. .	52
5.11	512 carbon atoms in liquid phase after 5000 MD steps. . . . .	53
5.12	Coordination numbers of 512 carbon atoms in liquid phase after 5000 MD steps. The number indicate the initial seeds of the randomization.	53
5.13	Coordination numbers of 512 carbon atoms in liquid phase superim- posed to the starting state. The number indicate the initial seeds of the randomization. . . . .	54
5.14	Coordination numbers of 512 carbon atoms in liquid phase after 10000 MD steps. The number indicate the initial seeds of the randomization.	54
5.15	512 carbon atoms in liquid phase after 10000 MD steps. . . . .	55
5.16	DOS calculation for a-C. . . . .	57
5.17	Detailed comparison between DOS calculation and NEXAFS results for amorphous carbon. . . . .	58
5.18	Two views of 512 carbon atoms in an amorphous configuration. . . .	58
5.19	Two views of sample preparation of an amorphous sphere embedded in a diamond matrix. 512 carbon atoms still in the original diamond configuration. The bonded atoms in blue are mobile. The other are pinned. . . . .	60
5.20	Three views of 512 carbon atoms after liquidizing and quenching a centered sphere. All the atoms displayed in left and center pictures. Not bonded atoms are pinned. In the right picture only mobile atoms are displayed. . . . .	61
5.21	DOS of a-C sphere in a diamond. . . . .	62
5.22	Diamond and various mixed samples comparison . . . . .	63
5.23	Diamond, mixed and a-C DOS comparison . . . . .	63

5.24	Hydrogen caged in 512 carbon atoms in a Diamond configuration. On the left, a sample with one hydrogen atom. A sample with four hydrogen atoms is shown in the right picture. Hydrogen atoms are painted in green. . . . .	64
5.25	DOS calculation for a Diamond with an H atom and LDOS for regular and hydrogenated atoms. . . . .	65
5.26	DOS comparison between one and four hydrogen atoms. . . . .	65

# List of Tables

5.1	Nearest neighbors in the liquid phase after 10K steps. . . . .	55
5.2	Nearest neighbors for different seeds. . . . .	56
5.3	sp2/sp3 ratio for different seeds. . . . .	56
5.4	Hybridization states in the sample for the melted-quenched sphere sample. . . . .	61
5.5	Hybridization number of the atoms inside the amorphous sphere. . . .	62





# Abstract

Carbon structures were simulated in order to deepen understanding of the properties of nanodiamond films. These properties were compared with the experimental results of different techniques, such as Near Edge X-ray Absorption Fine Structure (NEXAFS). The simulation was done by tight-binding methods for samples of hundreds of atoms.

It is experimentally observed that Chemical Vapor Deposition (CVD) nanodiamond films grow by deposition of hydrocarbon rich plasma presenting a structure of nanodiamond cores embedded in amorphous carbon. Consistent computational simulations of these structures, where it is possible to calculate physical processes in them, are required in order to deepen understanding of the processes leading to the growth of nanodiamond films. Specifically, Density Of States (DOS) calculations when compared with the experimental results from NEXAFS measurements enable us to interpret the NEXAFS characteristics. Our DOS calculations were in good agreement with experimental NEXAFS results.

New computational techniques, making possible larger and more accurate simulations were developed during this thesis. A new characterization method for carbon hybridization states was developed, leading to improved visualization of the samples, in order to give new insights into the comprehension of the sample geometry.

A technique to simulate a geometrical structure of nanodiamond cores embedded in amorphous carbon was developed in order to simulate nanodiamond film growth in CVD conditions as observed experimentally at the Technion. Initial studies of hydrogenated samples were made and some studies of their stability and DOS were carried out.

# Chapter 1

## Introduction

### 1.1 Carbon allotropes

The stable bonding configuration of carbon at ambient conditions is graphite, with an energy difference between graphite and diamond of  $\approx 0.02$  eV per atom. Due to the high energetic barrier between the two phases of carbon, the transition from diamond to the stable phase of graphite is very slow at normal conditions. This transition can also occur more rapidly, for example when diamond is exposed to ion bombardment or high temperature.

In the reverse direction, there are two main methods to produce synthetic diamond from graphite. The original method is High Pressure High Temperature (HPHT). This is the most widely used method because of its relative low cost. It uses large presses that can weigh a couple of hundred tons to produce a pressure of 5 GPa at 1,500 degrees Celsius to reproduce the conditions that create natural diamond inside the Earth. Another technique of HPHT synthesis of diamond from carbonaceous materials makes use of the short time compression and high temperatures achievable

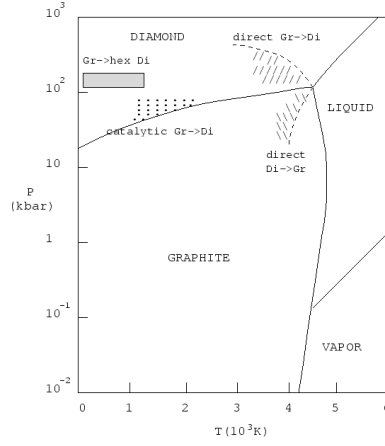


Figure 1.1: P, T phase diagram of carbon reproduced from [1].

during detonation. Various types of carbonaceous precursors can be used in this detonation process, including graphite, carbon black, fullerenes, organic substances, but amongst these graphite is the most widely used. The second method, using chemical vapor deposition or CVD, was invented in the 1980s, and does not require high pressure and high temperature conditions to create diamond crystallites. This is basically a method which creates a carbon plasma on top of a substrate onto which the carbon atoms deposit to form diamond.

In the diamond lattice, each carbon atom has four valence electrons spread in the  $s$  and  $p$  orbitals, the  $s$  orbital mixes with the three  $p$  orbitals ( $p_x$ ,  $p_y$ ,  $p_z$ ) forming  $sp^3$  hybridization, creating a strong tetrahedral structure. The four valence electrons of the carbon are equally distributed among the  $sp^3$  orbitals, each orbital pointing to one of the corners of a tetrahedron. This tetrahedral structure gives strength and stability to the bonds.

In the graphite lattice, the  $s$  orbital mixes with only two  $p$  orbitals forming three  $sp^2$  orbitals pointing to vertices of a triangle in plane. Three electrons occupy these

orbitals and together with the one electron left in the  $p$  orbital perpendicular to the  $sp^2$  plane contribute to conduction. Overlapping between  $sp^2$  orbitals of neighboring atoms in the same plane occur, also overlapping with their unhybridized  $p$  orbital resulting in a  $\pi$  bond. The whole structure is made of sheets held together by weak Van der Waals forces, separated by a distance of 3.40Å, giving softness to the structure.

Bridging between these two main allotropes of carbon (diamond and graphite) lie a whole variety of carbon materials which include, among others, amorphous  $sp^2$  bonded carbon (such as thermally evaporated carbon), micropolycrystalline  $sp^2$  bonded graphite (such as glassy carbon), nanodiamond films, and amorphous  $sp^3$  bonded carbon (sometimes referred to as amorphous diamond), which is structurally analogous to amorphous Si and is formed during low energy carbon ion deposition.

Another polymorphic form of carbon was discovered in 1985. It exists in discrete molecular form, and consists of a hollow spherical cluster of carbon atoms. Each molecule is composed of groups of sixty and more carbon atoms, bonded one to another, making both hexagonal and pentagonal geometrical configurations. The material composed of  $C_{60}$  is known as buckminsterfullerene, named in honor of R. Buckminster Fuller, who invented the geodesic dome. In the solid state, the  $C_{60}$  units form a crystalline structure and pack together in a face-centered cubic array [6]. The discovery that carbon could form stable, ordered structures other than graphite and diamond stimulated researchers worldwide to search for other new forms of carbon. The Japanese scientist Sumio Iijima discovered fullerene-related carbon nanotubes in 1991. The bonding in carbon nanotubes is  $sp^2$ , the tubes can therefore be considered as rolled-up graphitic sheets [7]. Carbon nanotubes exhibit extraordinary strength and unique electrical properties, and are efficient conductors of heat, that make them potentially useful in a wide variety of applications in nanotechnology, electronics,

optics, and other fields of materials science.

## 1.2 Diamond

Atomic carbon has an atomic number of 6 and a  $1s^2 2s^2 2p^2$  electronic ground state configuration. The carbon atom's electronic configuration is believed to change its ground state in diamond as introduced above and below visualized as follows:

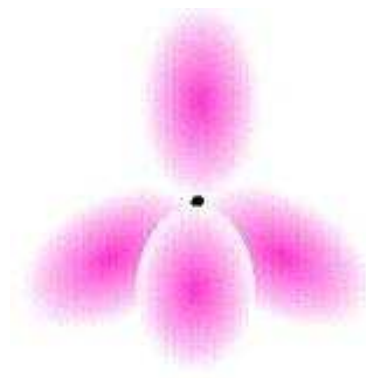


Figure 1.2: Representation of  $sp^3$  hybridization

If a carbon atom enters into the structure of diamond its two  $2s$  and  $2p$  electrons redistribute into four new equal-energy-level orbitals called  $2(sp^3)$  hybrid orbitals. It requires a loss of energy but this effect is compensated by a very profitable covalent bonding. The angular distribution of the wave functions for these four  $2(sp^3)$  orbitals can be illustrated by drawing four lobes whose axes are at  $109^\circ 28'$  to each other, the axes of these lobes thus extend toward the corners of an imaginary tetrahedron centered around the carbon atom, as shown in Figure 1.2.

Quantum-mechanical calculations indicate that greater overlap between orbitals

results in a stronger covalent bond. The diamond structure represents a three-dimensional network of strong covalent bonds, which explains why diamond is so hard. The diamond structure is cubic with a cube edge length of  $a_0 = 3.567$  Angstroms and can be viewed as two interpenetrating FCC structures displaced by  $(1/4, 1/4, 1/4)a_0$ . The diamond crystal is highly symmetric with a cubic space group  $F4_1/d \bar{3} 2/m = Fd\bar{3}m = O_h^7$ .

Since all the valence electrons contribute to the covalent bond, they are not free to migrate through the crystal and thus, diamond is a poor conductor with a bandgap of 5.48 eV.

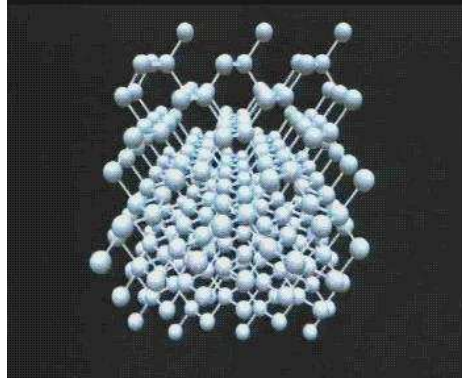


Figure 1.3: Visualization of a diamond lattice.

## 1.3 Graphite

In going from its ground state to the graphite structure, a carbon atom's electronic configuration as introduced above is believed to change as follows:

Three of the two  $2s$  and two  $2p$  electrons in carbon's ground state redistribute into three hybrid  $2(sp^2)$  orbitals which are a mathematical mixing of the  $s$  orbitals with

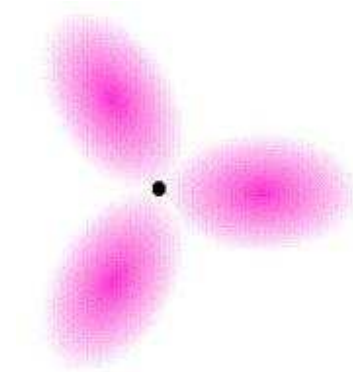


Figure 1.4: Representation of  $sp^2$  hybridization

two of the three  $p$  orbitals. The angular probabilities for these  $2(sp^2)$  orbitals can be represented by three coplanar lobes at  $120^\circ$  to each other. The fourth electron of the original two  $2s$  and two  $2p$  electrons fills that  $p$  orbital which does not participate in the  $2(sp^2)$  hybrid, the lobe for this  $p$  orbital being perpendicular to the plane defined by the three  $2(sp^2)$  orbitals, as shown in Figure 1.4.

In the graphite structure, overlap occurs between the  $2(sp^2)$  orbitals of neighboring atoms in the same plane. For such neighbors a side-to-side overlap also occurs between their unhybridized  $p$  orbitals. A side-to-side bonding known as  $\pi$ -bonding results between these neighbors. The electrons participating in this  $\pi$ -bonding seem able to move across these  $\pi$ -bonds from one atom to the next. This feature explains the graphite's ability to conduct electricity along the sheets of carbon atoms parallel to the (0001) direction. The in-plane nearest-neighbor distance is 1.421 Angstroms normal to (0001), adjacent sheets of carbon atoms are held together by the weak Van der Waals bonds and separated by a distance 3.40 Angstroms. This gives softness to the structure [8] [9]. The crystal structure is describes by hexagonal lattice with  $D_{6h}^4$  ( $P6_3/mmc$ ) space group. A graphite model is shown in Figure 1.5



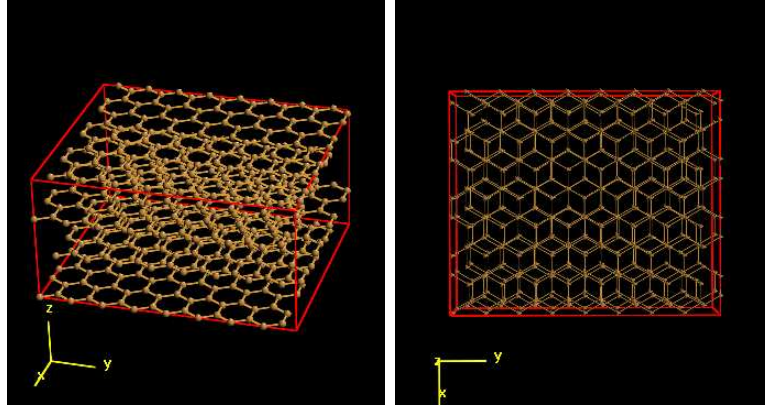


Figure 1.5: Perspective and normal views of a graphite model. Note the interlock of the planes on the right picture.

## 1.4 Graphene

Graphene is a one-atom-thick planar sheet of  $sp^2$  bonded carbon atoms that are densely packed in a honeycomb crystal lattice. The carbon-carbon bond length in graphene is approximately 0.142 nm. Graphene is the basic structural element of all carbon allotropes including graphite, carbon nanotubes and fullerenes. Perfect graphenes consist exclusively of hexagonal cells; pentagonal and heptagonal cells constitute defects. A graphene model can be seen in Figure 1.6.

## 1.5 Amorphous structures

The amorphous structure is characterized by a high degree of short range order and the absence of long range order. The short range order in amorphous structures can be seen in bond length, number of nearest neighbor atoms as well as in the angle between two bonds. At a longer range, there is no periodicity in the amorphous structure, hence its symmetry is broken, giving isotropic characteristics to the structure.

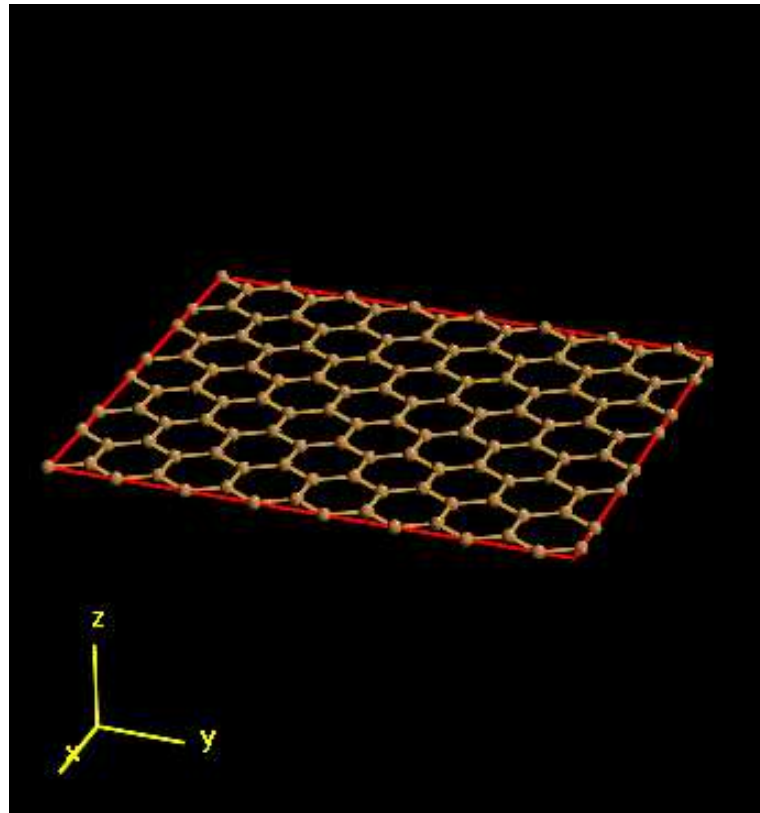


Figure 1.6: One graphene sheet.

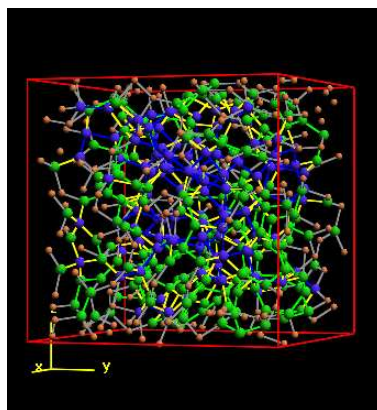


Figure 1.7: Amorphous carbon model.  $sp^2$  bonds are colored in green,  $sp^3$  in blue.

Energetically, atoms in the amorphous structure are not bonded ideally hence, the energy of the amorphous structure is higher than of a pure crystal. An amorphous model is shown in Figure 1.7. The method of preparation of amorphous diamond strongly affects the properties of the structure.

Two specific amorphous forms of carbon commonly appear and can be distinguished by their microscopic and macroscopic properties:

1. Diamond-like amorphous carbon, usually denoted by  $ta - C$  is characterized by a mean number of nearest neighbors (or coordination number),  $z = 3.5 - 3.8$ , mean bond angle of  $110 - 115^\circ$  and a density of  $2.9 - 3.5 \text{ gr/cm}^3$ . This  $ta - C$  is a hard, dense material mostly made of distorted  $sp^3$  bonds.
2. Graphite-like amorphous carbon, usually denoted by  $a - C$  is characterized by high percentage,  $\sim 70\%$  to  $\sim 98\%$ , of  $sp^2$  bonds hence, a mean number of nearest neighbors,  $z = 2.9 - 3.2$ , a bond angle of around  $120^\circ$  and a density of  $2.0 - 2.7 \text{ gr/cm}^3$ . This  $a - C$  is a soft, opaque material mostly made of distorted  $sp^2$  bonds.

## 1.6 Objectives

In this study we build new models, that allow studies of the role of hydrogen in the growth of nano diamond films and get new insights of the physical and chemical properties of these films. These models are more complicated than those required to describe regular carbon structures, and therefore need a new machinery which

includes the development of new tools for calculation, manipulation and visualization of the samples.

In addition, and based on the machinery developed in this research thesis, we investigate the relation between calculated Density of States (DOS) of carbon models with experimental results of NEXAFS measurements. Different allotropes of carbon like graphite, graphene and diamond will be studied to assert the validation of the physical models and techniques.

# Chapter 2

## Experimental techniques

### 2.1 NEXAFS

NEXAFS (Near Edge X-ray Absorption Fine Structure) [10] is an element-specific electron spectroscopic technique which is highly sensitive to bond angles, bond lengths and the presence of adsorbates. NEXAFS selects a specific atomic species and probes its bonds to intra-molecular and, to a lesser degree, extra-molecular (i.e., surface atom) neighbors.

Among its capabilities are: the ability to detect the presence of specific bonds in molecules (e.g., C-C, C-H bonds in hydrocarbons), the determination of the lengths of these intra-molecular bonds and the derivation of the precise orientation of molecules and functional groups on surfaces or in solids. By comparison with spectra for free and chemisorbed molecules NEXAFS can also reveal which orbitals are involved in the chemisorption bond. To first order it gives no information on the detailed atomic adsorbate-substrate registry. This part of the problem can, however, be solved with

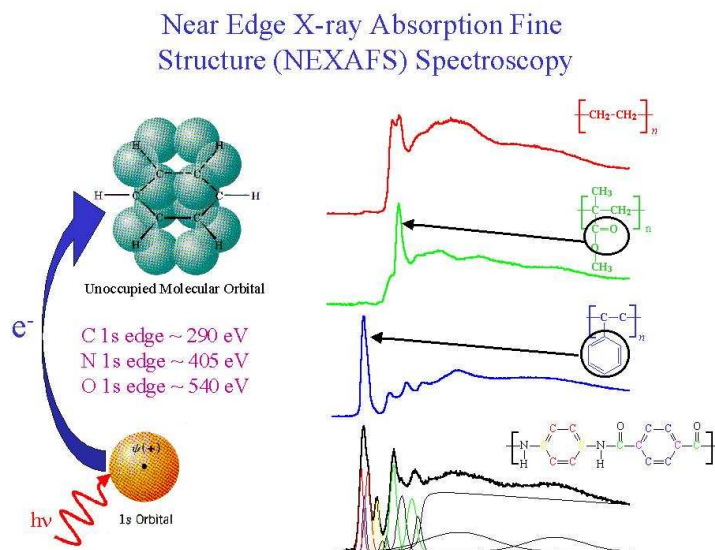


Figure 2.1: Basic process (left) and composition (right) of the NEXAFS spectra. [2]

related and complementary surface extended X-ray absorption fine structure (SEXAFS) technique. A qualitative explanation of the NEXAFS spectrum is shown in Figure 2.1.

When X-rays pass through any sort of material, a percentage of them will be absorbed. Measuring the amount of absorption with increasing X-ray energy reveals so-called edge structures, where the level of absorption suddenly increases. This happens when an X-ray has sufficient energy to free or excite a bound electron within the material. Usually, small oscillations can be seen superimposed on the edge step. These gradually die away as the X-ray energy increases.

The oscillations, which occur relatively close to the edge (within about 40 eV) are known as NEXAFS (Near Edge X-ray Absorption Fine Structure) or XANES (X-ray Absorption Near Edge Structure). The term XANES is more commonly used for solids and inorganic complexes while NEXAFS is used more in conjunction with

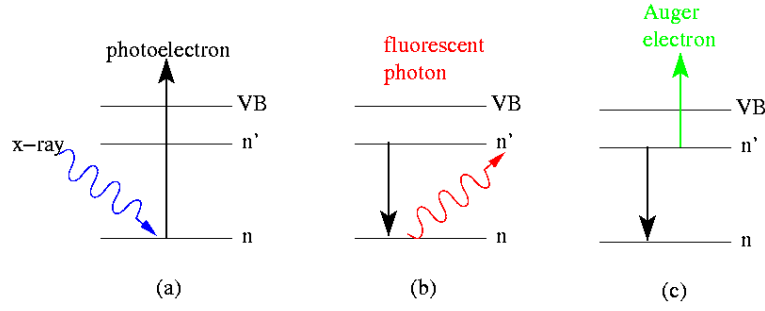


Figure 2.2: NEXAFS fundamental phenomena. [3]

surfaces. NEXAFS by convention is usually reserved for soft X-ray spectroscopy (photon energy less than 1000 electron volts). NEXAFS is distinguished from the closely related EXAFS (Extended X-ray Absorption Fine Structure) method in that NEXAFS concentrates on fine structure within about 30 eV of the absorption edge while EXAFS considers the extended spectrum out to much higher electron kinetic energies (hundreds of electron volts past the edge).

### 2.1.1 Theory

The fundamental phenomenon underlying NEXAFS is the absorption of an x-ray photon by a core level of an atom in a solid and the consequent emission of a photoelectron. The NEXAFS principle is based on the determination of the x-ray absorption coefficient depending on the photon energy at a fixed angle of illumination. As the optical excitation of a core level electron requires the binding energy as a minimum photon energy, the transgression of this energy will coincide with an increased absorption coefficient. This leads to the formation of absorption edges, which may be indexed by their atomic subshells (K,L,M...).

The fundamental processes which contribute to NEXAFS spectra are: (a) photoabsorption of an x-ray into a core level followed by photoelectron emission, followed by either (b) filling of the core hole by an electron of another level, accompanied by fluorescence; or (c) filling of the core hole by an electron of another level followed by emission of an Auger electron. This phenomena is illustrated in Figure 2.2

The resulting core hole is filled either via an Auger process or by capture of an electron from another shell followed by emission of a fluorescent photon.

The difference between NEXAFS and traditional photoemission experiments is that in photoemission, the initial photoelectron itself is measured, while in NEXAFS the fluorescent photon or Auger electron or an inelastically scattered photoelectron may also be measured. While direct photoemission spectroscopy offers an experimental approach to the occupied electronic bands of a solid state, NEXAFS is a technique to characterize surfaces by evaluation of unoccupied electronic states.

The distinction sounds trivial but is actually significant: in photoemission the final state of the emitted electron captured in the detector must be an extended, free-electron state. By contrast in NEXAFS the final state of the photoelectron may be a bound state such as an exciton since the photoelectron itself need not be detected.

Only sufficient photon energy enables the photoexcitation of a core level electron beyond the Fermi level  $E_f$ . After  $10^{-14}s$  the ionized atom may relax by occupation of the core hole with an electron from the valence band (VB), while the generated energy will normally not be used for the emission of a fluorescence photon (probability 1 %), but will be absorbed for the vacuum emission of an Auger electron (probability 99%) from the valence band. In case of insufficient energy for the emission of the primary electron, it may be excited into a conduction band (CB) level, so that a similar relaxation process becomes possible. This spectator process then results in



the emission of only one Auger electron.

Following the excitation of a core level electron several ways of relaxation are possible. Secondary electrons are generated which undergo multiple scattering processes before they leave the crystal structure as low-energy photoelectrons. The effect of measuring fluorescent photons, Auger electrons, and directly emitted electrons is to sum over all possible final states of the photoelectrons, meaning that what NEXAFS measures is the total joint density of states of the initial core level with all final states, consistent with conservation rules. The distinction is critical because in spectroscopy final states are more susceptible to many-body effects than initial states, meaning that NEXAFS spectra are more easily calculable than photoemission spectra. Due to the summation over final states, various sum rules are helpful in the interpretation of NEXAFS spectra.

When the x-ray photon energy resonantly connects a core level with a narrow final state in a solid, such as an exciton, readily identifiable characteristic peaks will appear in the spectrum.

## 2.2 Diamond nucleation with hydrogen

The diamond phase of carbon is always contaminated with hydrogen, whether it is natural or an artificial polycrystalline diamond obtained by Chemical Vapor Deposition (CVD). In recent years, high-pressure, high-temperature chemical vapor deposition production of diamond has been developed to facilitate diamond growth at sub-atmospheric pressures [11], typically applying a hydrocarbon-hydrogen plasma over a silicon substrate held at  $\sim 1000^\circ$  to  $1100^\circ\text{K}$  while being negatively biased to  $\sim 100$  to  $200\text{V}$  (Bias Enhanced Nucleation, BEN). Diamond growth on diamond is

relatively well understood and controlled, while diamond growth on silicon requires a nucleation step that is much less understood and relies largely on trial and error.

A model proposed by Y. Lifshitz et al. proposed a mechanism of diamond nucleation from energetic species as carbon, hydrocarbon and hydrogen originated from the chemical vapor deposition (CVD) plasma [12]. The model is composed of 4 steps:

1. The first step is the formation of amorphous hydrogenated carbon (a-C:H) on a silicon substrate via a subplantation process, where the energetic carbon, hydrocarbon and hydrogen atoms bombard the surface and are subsequently stopped and incorporated in subsurface layers. Carbon interstitials and hydrogen atoms are provided through the subimplantation process.
2. The second stage is the precipitation of  $sp^3$  carbon clusters induced by a “thermal spike” (where energy is deposited on the carbon electrons by the energetic hydrogen atoms, consequently, the electrons transform the energy to the lattice atoms by an electron-lattice interaction leading to the increase of temperature) . Most clusters are amorphous but a few are perfect diamond.
3. The third step consists of the annealing of faults in defective clusters by the incorporation of carbon “interstitials” in reactive sites and by hydrogen termination. The amorphous matrix contain  $\sim 20$  to 30% of hydrogen.
4. The last step is the transformation of amorphous carbon to diamond at the amorphous matrix-diamond interface. This growth of the diamond clusters is typically up to several nm in size( $10^4$  to  $3 \times 10^4$  atoms). This transformation is induced by a “preferential displacement” mechanism caused by impact of energetic hydrogen atoms.

Each step of this mechanism is supported by previously reported experiments [11] and [13] carried out using a direct-charge glow discharge methane-hydrogen plasma incorporated hot filament chemical vapor deposition (HFCVD) on a negatively biased Si (100) at 800° to 950°C followed by HFCVD growth.



# Chapter 3

## Simulation Techniques

In this section existing methodology is reviewed and some of the new techniques developed in this research are introduced.

### 3.1 Ab-initio

*Ab-initio*, from Latin, 'From the beginning'. The Ab-initio technique is based on first-principles density functional theory, without any adjustable parameters, hence, is known to be generalized, reliable and accurate. This technique involves the solution of the Schrodinger equation for each electron in the system, in the self-consistent potential created by the other electrons and by the nuclei. This method is known to be very expensive in terms of Central Processing Unit (CPU) time.

### 3.2 LCAO calculations

In atoms the electrons are tightly bound to their nuclei. If the atoms are so close that their separations become comparable to the lattice constant in solids, their wave

functions will overlap. We will approximate the electronic wave functions in the solid by linear combinations of the atomic orbitals. This approach is known as the tight-binding approximation or Linear Combinations of Atomic Orbitals (LCAO) approach.

In covalently bonded semiconductors the valence electrons are concentrated mainly in the bonds. Therefore the valence electrons wave functions should be very similar to bonding orbitals found in molecules. In addition to being a good approximation for calculating the valence bond structure, the LCAO method has the advantage that the band structure can be defined in terms of a small number of overlap parameters. The overlap parameters have a simple physical interpretation as representing interactions between electrons on adjacent atoms. While the method has been utilized by many authors, the approach we will describe follows that of Chadi and Cohen [14].

The position of an atom in the primitive cell denoted by  $j$  will be decomposed into  $r_{jl} = R_j + r_l$ , where  $R_j$  denotes the position of the  $j$ th primitive cell of the Bravais lattice and  $r_l$  is the position of the atom  $l$  within the primitive cell. Let  $h_l(r)$  denotes the Hamiltonian for the isolated atom  $l$  with its nucleus chosen as the origin. The Hamiltonian for the atom located at  $r_{jl}$  will be denoted  $h_l(r - r_{jl})$ . The wave equation for  $h_l$  is given by

$$h_l \phi_{ml}(r - r_{jl}) = E_{ml} \phi_{ml}(r - r_{jl}),$$

where  $E_{ml}$  and  $\phi_{ml}$  are the eigenvalues and eigenfunctions of the state indexed by  $m$ . The atomic orbitals  $\phi_{ml}$  are known as Löwdin orbitals [15]. They have been constructed in such a way that wave functions centered at different atoms are orthogonal to each other. We assume that the Hamiltonian for the crystal  $\mathcal{H}$  is equal to the sum of the atomic Hamiltonians and a term  $\mathcal{H}_{int}$  which describes the interaction between the different atoms. We further assume the interaction between the atoms to be weak so that  $\mathcal{H}$  can be diagonalized by perturbation theory. In this approximation the

unperturbed Hamiltonian  $\mathcal{H}_0$  is simply

$$\mathcal{H}_0 = \sum_{j,l} h_l(r - r_{jl})$$

and we can construct the unperturbed wave functions as linear combinations of the atomic wave functions. Because of the translational symmetry of the crystal, these unperturbed wave functions can be expressed in the form of Bloch functions:

$$\Phi_{mlk} = \frac{1}{\sqrt{N}} \sum_j \exp(ir_{jl} * k) \phi_{ml}(r - r_{jl}),$$

where  $N$  is the number of primitive unit cells in the crystal. The eigenfunctions  $\Psi_k$  of  $\mathcal{H}$  can be written as linear combinations of  $\Phi_{mlk}$ :

$$\Psi_k = \sum_{ml} C_{ml} \Phi_{mlk}.$$

To calculate the eigenfunctions and eigenvalues of  $\mathcal{H}$ , we operate on  $\Psi_k$  with the Hamiltonian  $\mathcal{H} = \mathcal{H}_0 + \mathcal{H}_{int}$ . From the orthogonality of the Bloch functions we obtain a set of linear equations in  $C_{ml}$ :

$$\sum_{ml} (H_{ml,m'l'} - E_k \delta_{mm'} \delta_{nn'}) C_{m'l'}(k) = 0,$$

where  $H_{ml,m'l'}$  denotes the matrix element  $\langle \Phi_{mlk} | \mathcal{H} | \Phi_{m'l'k} \rangle$  and  $E_k$  are the eigenvalues of  $\mathcal{H}$ . When we substitute the wave function  $\Psi_{mlk}$  we obtain

$$\begin{aligned} H_{ml,m'l'}(k) &= \sum_j \sum_{j'} \frac{\exp[i(r_{jl} - r_{j'l'}) * k]}{N} * < \Psi_{mlk}(r - r_{jl}) | \mathcal{H} | \Psi_{m'l'k}(r - r_{j'l'}) > \\ &= \sum_j \exp[i(R_j + r_l - r_{l'}) * k] * < \psi_{mlk}(r - r_{jl}) | \mathcal{H} | \psi_{m'l'k}(r - r_{j'l'}) > \end{aligned}$$

Instead of summing  $j$  over all the unit cells in the crystal, we will sum over the nearest neighbors only. In the diamond crystal this means  $j$  will be summed over the atom itself plus four nearest neighbors.

The matrix elements  $\langle \psi_{mlk}(r - r_{jl}) | \mathcal{H} | \psi_{m'l'k}(r - r_{j'l'}) \rangle$  can be expressed in terms of overlap parameters for two diamond atoms. As it will be shown below, for a homopolar molecule, there are only four nonzero overlap parameters. The band structure can now be obtained by diagonalizing the Hamiltonian for different values of  $k$ .

### 3.3 Molecular dynamics

Molecular Dynamics is a computer simulation technique where the time evolution of a set of interacting atoms is followed by integrating their equations of motions in a classical many-body system. The classical contribution is that the motion of the constituent particles obeys the laws of classical mechanics, notably  $F = ma$ , the Newton equations are solved for each atom participating in the simulation. This technique is deterministic: given an initial set of positions and velocities, the subsequent time evolution is in principle determined.

#### 3.3.1 Semi-empirical potentials

Usually the potentials which are used in the Molecular Dynamics simulation are derived directly from observed experiments (such is the case in the Lennard-Jones potential or the classical Coloumb), or by ab-initio calculations. The ultimate goal, is the reduction of the computational expense for molecular dynamics simulation with a quantum mechanical potential energy function.

The question of potentials is a delicate and controversial one. The same issue arises in the context of molecular statics or in the use of simulated annealing to find optimum configurations at a particular temperature. Obviously, the best *potential* is



found from a quantum mechanical study. This can only be done for a system of very limited size, and extremely limited time development. Next best is something in the spirit of *tight-binding* molecular dynamics (see below), followed by manybody potentials assembled from first principle results and experimental measurements. Excellent agreement between manybody potentials and first principle results can be found even for the case of carbon, which is not an easy system to model because of the different bonding configurations. Saada, Adler and Kalish [4] found such agreement in a series of calculations concerning the surface graphitization of diamond with judicious use of Tersoff/Brenner manybody potentials. The weakest potentials for general use are the simple potentials, such as Lennard-Jones. These are great for argon, but do not give a good approximation to semiconductors or ceramics. However they do enable study of large samples for long times, development of new molecular dynamics techniques and validation of temperature maintenance algorithms. Sometimes empirical corrections were made for the potentials for specific elements. Tersoff [16] and Stillinger-Weber [17] are other common choices for potentials.

### 3.3.2 Tight binding molecular dynamics

Tight-binding molecular dynamics [18] is a useful method for studying the structural, dynamical, and electronic properties of covalent systems. The method incorporates electronic structure calculation into molecular dynamics through an empirical tight-binding Hamiltonian and bridges the gap between ab initio molecular dynamics and simulations using empirical classical potentials.

### 3.3.3 The tight-binding model

The Hamiltonian of a system of ion cores and valence electrons can be written as:

$$H = T_i + T_e + U_{ee} + U_{ei} + U_{ii} \quad (3.1)$$

where  $T_{i,e}$  is the kinetic energy of ions and electrons respectively;  $U_{ee}$ ,  $U_{ei}$ ,  $U_{ii}$  are the electron-electron, electron-ion and ion-ion interactions. For a single electron, the many-body Hamiltonian, (3.1), can be reduced to an electron moving in the average field due to other valence electrons and due to the ion fields. We can do this because electrons move  $\sim 10^2 - 10^3$  faster than ions and each electron moves independently of the other electrons in the system [19], and experiences an effective interaction due to the other electrons and the ions.

Let  $h$  be the reduced one-electron Hamiltonian

$$h = T + U_{ee} + U_{ei} \quad (3.2)$$

$|\Psi_n\rangle$  is the  $n^{\text{th}}$  eigenfunction corresponding to the  $n^{\text{th}}$  eigenvalue,  $\epsilon_n$  such that

$$h|\Psi_n\rangle = \epsilon_n|\Psi_n\rangle \quad (3.3)$$

Here, we represent the wavefunctions  $|\Psi_n\rangle$  as linear combination of atomic orbitals  $|\phi_{l\alpha}\rangle$ :

$$|\Psi_n\rangle = \sum_{l\alpha} c_{l\alpha}^n |\phi_{l\alpha}\rangle \quad (3.4)$$

where  $l$  is the quantum number index and  $\alpha$  labels the ions. The  $c_{l\alpha}^n$  coefficients represent the occupancy of the  $l^{\text{th}}$  orbital located at the  $\alpha^{\text{th}}$  site. In the general case, the  $|\phi_{l\alpha}\rangle$  basis is not orthogonal:

$$\langle\phi_{l\alpha}|\phi_{l'\beta}\rangle \neq 0 \quad (3.5)$$

Substituting (3.5) into (3.3), multiplying from the left and remembering that  $h$  is not necessarily diagonalized we introduce the overlapping integrals  $S$  and we get the secular problem,

$$\sum_{l\alpha} \langle \phi_{l'\beta} | h | \phi_{l\alpha} \rangle c_{l\alpha}^n = \sum_{l\alpha} \epsilon_n (\delta_{ll'} \delta_{\alpha\beta} + S_{ll',\alpha\beta}) c_{l\alpha}^n \quad (3.6)$$

From a numerical point-of-view, the secular problem (3.6) corresponds to a generalized linear problem,

$$hc^n = \epsilon_n (S + I) c^n \quad (3.7)$$

where  $I$  is the identity matrix, and  $S$  is given by

$$S_{ll',\alpha\beta} = \langle \phi_{l'\beta} | \phi_{l\alpha} \rangle - \delta_{ll'} \delta_{\alpha\beta} \quad (3.8)$$

which represents the non-orthogonal tight-binding model. The use of such model in a large-scale simulation is not numerically convenient and is very time consuming, since the evaluation of the overlapping integrals is needed at each time step of the simulation and is extremely computational workload. According to Löwdin the non-orthogonality can be removed, by using a new set of orthogonal atomic orbitals  $|\varphi_{l\alpha}\rangle$ . By doing so we reduce the secular problem to be

$$hb^n = \epsilon_n b^n \quad (3.9)$$

where  $b^n = \{b_{l\alpha}^n\}$  are the new coefficients of the linear combination,

$$|\Psi_n\rangle = \sum_{l\alpha} b_{l\alpha}^n |\varphi_{l\alpha}\rangle \quad (3.10)$$

and orthogonality,

$$\langle \varphi_{l'\beta} | \varphi_{l\alpha} \rangle = \delta_{ll'} \delta_{\alpha\beta} \quad (3.11)$$

Löwdin orbitals  $|\varphi_{l\alpha}\rangle$  preserve the properties of the original non-orthogonal basis  $|\phi_{l\alpha}\rangle$ .

The lattice is broken into primitive cells and the position for an atom in the primitive cell  $j$  is decomposed into  $r_{jl} = R_j + r_l$ , where  $R_j$  denotes the position of the  $j^{\text{th}}$  primitive cell. When we have perfect crystals with translational symmetry, we can further enhance Löwdin equations and express our wave functions in the form of Bloch functions

$$|\Phi_{kl\alpha}\rangle = \frac{1}{\sqrt{N}} \sum_j \exp(ir_{jl} \cdot k) \varphi_{l\alpha}(r - r_{jl}) \quad (3.12)$$

Here we have a summation over all primitive cells  $j$  in our lattice,  $l$  is the orbital of the  $\alpha^{\text{th}}$  site and  $N$  is the total number of primitive unit cells in the crystal.

The calculation of the orthogonal tight-binding model is still computationally heavy, and some approximations must be made for the calculation to be time-effective. The off-diagonal matrix elements of  $\langle \varphi_{l'\beta} | h | \varphi_{l\alpha} \rangle$ ,  $l\alpha \neq l'\beta$ , are the *hopping integrals*, and the on-site elements  $\langle \varphi_{l\alpha} | h | \varphi_{l\alpha} \rangle$ , are the atomic orbital energies. In the tight-binding approach these are constants to be fitted using the following approximations:

1. We use a *minimal basis set* for only the atomic orbitals whose energy is close to that of the energy bands that we are interested in [20]. Hence, in the diamond simulations we used only the  $2s$  (one orbital) and  $2p$  (three orbitals:  $p_x$ ,  $p_y$  and  $p_z$ ) orbitals to describe the occupied bands.
2. We consider hopping integrals between two atoms separated by a distance shorter than a suitable cutoff. Obviously, this must be done to reduce the number of parameters to be fitted and a cut-off which includes the nearest neighbors is appropriate. However, Lowdin functions extend further than the

non-orthogonal functions because the orthogonalization procedure involves orbitals from nearby atoms hence, interactions extending beyond the first nearest neighbors have to be taken into account when an orthogonal basis is used.

Using these approximations, the off-diagonal matrix elements of the Hamiltonian are fitted to the electronic band structure of the equilibrium crystal phase, These matrix elements are known and were calculated from first principle models. Sets of these hopping integrals can thus be obtained for each crystalline structure considered.

### 3.3.4 Energy calculations

Once the single-particle energies are known by solving the secular problem given in (3.9), the total potential energy  $E_{tot}$  of a crystalline system of ion cores and valence electrons can be written as

$$E_{tot} = U_{ie} + U_{ii} + U_{ee} = 2 \sum_{k,n} f_{FD}[\epsilon_n(k), T] \epsilon_n(k) + U_{ii} - U_{ee} \quad (3.13)$$

where  $f_{FD}$  is the Fermi-Dirac distribution function and the  $-U_{ee}$  contribution corrects the double counting of the electron-electron interactions in the first term. The sum over all the single-particle energies is commonly known as the band structure energy,  $E_{bs}$

$$E_{bs} = 2 \sum_{k,n} f_{FD}[\epsilon_n(k), T] \epsilon_n(k) \quad (3.14)$$

with a factor of 2, to take into account the spin degeneracy. The last two terms appearing in (3.13) are commonly grouped together forming an effective repulsive potential  $U_{rep} = U_{ii} - U_{ee}$  which is assumed to be short-ranged because of the efficient dielectric screening occurring in semiconductor materials.

### 3.3.5 Rescaling functions

As mentioned, the elements of the Hamiltonian matrix are fitted to first principle calculations for different equilibrium structures [21]. To describe the properties of non-equilibrium structures, such as amorphous solids or liquids, the hopping integrals and the repulsive energy should be rescaled with respect to the interatomic distance.

Generally, the equilibrium hopping integral  $\langle \varphi_{l'\beta} | h | \varphi_{l\alpha} \rangle = h_{l'l}$  can be written as

$$h_{l'l}(R_{\alpha\beta}) = h_{l'l}^{(0)} f_{l'l}(R_{\alpha\beta}) \quad (3.15)$$

where  $f_{l'l}(R_{\alpha\beta})$  is a scaling function of two orbitals  $l$  and  $l'$  placed on the atoms at  $R_\alpha$  and  $R_\beta$ , respectively. The constraint on this rescaling function is that  $f_{l'l}(R^{(0)}) = 1$  for  $R^{(0)}$  is the equilibrium interatomic distance. The rescaling functions proposed by Goodwin et. al. [22] for Si and later improved for Carbon by Xu et. al. [23] greatly improve the transferability of the tight binding model to structures not included in the parameterization. For the rescaling of the hopping integrals

$$h(r) = h_0 \left(\frac{r_0}{r}\right)^n \exp\left\{n\left[-\left(\frac{r}{r_c}\right)^{n_c} + \left(\frac{r_0}{r_c}\right)^{n_c}\right]\right\} \quad (3.16)$$

and for the repulsive potential

$$\phi(r) = \phi_0 \left(\frac{d_0}{r}\right)^m \exp\left\{m\left[-\left(\frac{r}{d_c}\right)^{m_c} + \left(\frac{d_0}{d_c}\right)^{m_c}\right]\right\} \quad (3.17)$$

In these Goodwin rescaling functions, the parameters  $n_c$  and  $r_c$  are the same as  $m_c$  and  $d_c$  respectively, while with the Xu functions these parameters are not necessarily the same. All the parameters appearing in the rescaling functions were obtained by fitting first-principle results of the energy versus nearest-neighbor interatomic distance for different crystalline phases, giving equilibrium sets of hopping integrals for these structures. In this way, the tight-binding model is transferable to different atomic environments.

### 3.3.6 Simulation steps

During a MD (Molecular Dynamics) run we compute the interatomic forces  $F_\alpha$  (where  $\alpha = 1, \dots, N_{at}$ ) to move atoms and to generate trajectories the phase space. They can be evaluated from the Tight-Binding Molecular Dynamics Hamiltonian  $\mathcal{H}$

$$\mathcal{H} = \sum_{\alpha} \frac{p_{\alpha}^2}{2m_{\alpha}} + 2 \sum_n \epsilon_n f_{FD}(\epsilon_n, T) + U_{rep} \quad (3.18)$$

For our practical purpose in accordance with the adiabatic approximation, the electronic temperature is assumed to be zero, hence, equation (3.18) can be simplified to

$$\mathcal{H} = \sum_{\alpha} \frac{p_{\alpha}^2}{2m_{\alpha}} + 2 \sum_n^{(occup)} \epsilon_n + U_{rep} \quad (3.19)$$

where (occup) indicates that we just use the electron energies,  $\epsilon_n$  belonging to the lower half spectrum of the Tight-Binding matrix (3.6).

The force  $F_\alpha$  is then given by

$$F_\alpha = -\frac{\partial \mathcal{H}}{\partial R_\alpha} = -\frac{\partial}{\partial R_\alpha} 2 \sum_n^{(occup)} \epsilon_n - \frac{\partial}{\partial R_\alpha} U_{rep} \quad (3.20)$$

where the first term describes the attractive force and the second describes the repulsive term acting upon particle  $\alpha$ .  $U_{rep}$  is known analytically as a short-ranged function of the interatomic distance, and hence, computed trivially. The attractive force, however, is computed numerically using the Hellman-Feynman theorem [24]. By using Eq. (3.9) and Eq. (3.15), the attractive contribution acting upon atom  $\alpha$  can be calculated as

$$\begin{aligned} -\frac{\partial}{\partial R_\alpha} 2 \sum_n^{(occup)} \epsilon_n &= -2 \frac{\partial}{\partial R_\alpha} \sum_n^{(occup)} \langle \Psi_n | h | \Psi_n \rangle \\ &= -2 \frac{\partial}{\partial R_\alpha} \sum_n^{(occup)} \sum_{l'\gamma\beta} b_{l'\gamma}^n b_{l'\beta}^n \langle \varphi_{l'\gamma} | h | \varphi_{l'\beta} \rangle \end{aligned}$$

$$\begin{aligned}
&= -2 \frac{\partial}{\partial R_\alpha} \sum_n^{(occup)} \sum_{ll'\gamma\beta} b_{l\gamma}^n b_{l'\beta}^n h_{ll'}(R_{\gamma\beta}) \\
&= -2 \sum_n^{(occup)} \sum_{ll'\gamma\beta} b_{l\gamma}^n b_{l'\beta}^n h_{ll'}^{(0)} \frac{\partial}{\partial R_\alpha} f_{ll'}(R_{\gamma\beta})
\end{aligned} \tag{3.21}$$

Hence, the spectrum of the eigenvalues and eigenvectors of the Tight-Binding matrix need to be computed, respectively, the band-structure contribution to the total potential energy and the attractive contribution to the forces. The exact calculation must be done at every time-step of the simulation. Since the Tight-Binding matrix can be large, the computer memory holding the matrix must be large as well, and obviously, the simulation time might be long.

### 3.4 Annealing and quenching

Simulated Annealing is a stochastic computational technique derived from statistical mechanics for finding near-globally-minimum solutions to large optimization problems. In statistical mechanics, when a system of atoms, or molecules, is at equilibrium at a given temperature  $T$ , then the probability  $P_T(s)$  that the system is in a given configuration  $s$  depends upon the energy  $E(s)$  of the configuration and follows the Boltzmann distribution:

$$P_T(s) = \frac{\exp(-\frac{E(s)}{kT})}{\sum_i \exp(-\frac{E(i)}{kT})} \tag{3.22}$$

where  $k$  is the Boltzmann constant.

One can simulate the behavior of a system of particles in thermal equilibrium at temperature  $T$  using a stochastic relaxation technique developed by Metropolis et



al. [25] Suppose at time  $t$ , the system is in configuration  $q$ . A candidate  $r$  for the configuration at time  $t+1$  is generated randomly. The criterion for selecting or rejecting configuration  $r$  depends on the difference between the energies of configurations  $r$  and  $q$ . Specifically, one computes the ratio  $p$  between the probability of being in  $r$  and the probability of being in  $q$ :

$$p = \frac{P_T(r)}{P_T(q)} = \exp\left(-\frac{E(r) - E(q)}{kT}\right) \quad (3.23)$$

If  $p > 1$ , that is the energy of  $r$  is strictly less than the energy of  $q$ , then the configuration  $r$  is automatically accepted as the new configuration for time  $t + 1$ . If  $p \leq 1$ , that is, the energy of  $r$  is greater than or equal to that of  $q$ , then the configuration  $r$  is accepted as the new configuration with probability  $p$ . Thus, configurations of higher energies can be attained.

Since the probability that a step is accepted is a function of the temperature  $T$ , one can bring the configuration after a sufficient number of trials to a local or a global minimum energy, according to the temperature. Thus, on the basis of the method described above, the simulated annealing technique is applied to minimize the energy of a system by suitably changing the temperature.

In studying such systems of particles, one often seeks to determine the nature of the low energy states, for example, whether freezing produces crystalline or glassy solids. Very low energy configurations are not common, when considering the set of all configurations. However, at low temperatures they predominate, because of the nature of the Boltzmann distribution. To achieve low energy configurations, it is not sufficient to simply lower the temperature. One must use an annealing process,

where the temperature of the system is elevated, and then gradually lowered, spending enough time at each temperature to reach thermal equilibrium. If insufficient time is spent at each temperature, especially near the freezing point, then the probability of attaining a very low energy configuration is greatly reduced.

### 3.5 Density of states

In statistical and condensed matter physics, the density of states (DOS) of a system describes the number of states at each energy level that are available to be occupied [26]. A high DOS at a specific energy level means that there are many states available for occupation. A DOS of zero means that no states can be occupied at that energy level.

Waves, or wave-like particles, can only exist within quantum mechanical (QM) systems if the properties of the system allow the wave to exist. In some systems, the interatomic spacing and the atomic charge of the material allows only electrons of certain wavelengths to exist. In other systems, the crystalline structure of the material allows waves to propagate in one direction, while suppressing wave propagation in another direction. Waves in a QM system have specific wavelengths and can propagate in specific directions, and each wave occupies a different mode, or state. Because many of these states have the same wavelength, and therefore share the same energy, there may be many states available at certain energy levels, while no states are available at other energy levels.

### 3.6 k-sampling

For a periodic system, the  $\mathbf{k}$  points appearing in the wave function belong to the first Brillouin zone, by virtue of Bloch's theorem. In the case of samples with defects, which are by definition aperiodic, the cell that contains the defects is periodically repeated, using periodic boundaries. The Bloch theorem can be therefore applied to this supercell, the dimension of the Brillouin zone being determined by the dimension of the supercell itself, i. e. the larger the supercell, the smaller the Brillouin zone should be.

To calculate the energy band, or the charge density for example, the sum over these  $\mathbf{k}$  points has to be done. Therefore, choosing a sufficiently dense mesh of summation is crucial for the convergence of the results. Monkhorst and Pack [27] proposed a scheme where the  $\mathbf{k}$  points are distributed homogeneously in the Brillouin zone according to

$$\mathbf{k} = x_1 \mathbf{b}_1 + x_2 \mathbf{b}_2 + x_3 \mathbf{b}_3$$

where  $\mathbf{b}_1, \mathbf{b}_2, \mathbf{b}_3$  are the reciprocal lattice vectors, and

$$x_i = \frac{l}{n_i}, \quad l = 1, \dots, n_i$$

where  $n_i$  are the folding parameters.

Usually, total energies of different structures are compared. Therefore, if the two structures have the same unit cell, the same set of  $\mathbf{k}$ -points should be used. Since only the difference in the energies of the two structures is required, possible errors from a non-converged  $\mathbf{k}$ -point sampling may cancel out. The computational effort could therefore be reduced by using a carefully chosen and small  $\mathbf{k}$ -point set.

Alternative methods for choosing  $\mathbf{k}$ -point mesh were been proposed. Chadi and Cohen [28] proposed to choose the  $\mathbf{k}$ -point mesh on the basis of "shells" analysis.

### 3.7 Coordination number

Amorphous carbon solids ( $ta - C$  as well as  $a - C$ ) are characterized by the  $sp^3/sp^2$  ratio between fourfold atoms  $sp^3$  and treefold atoms  $sp^2$ . Each  $sp^3$  bonded atom has four nearest neighbors separated by a distance of approximately 1.54. Each  $sp^2$  bonded atom has only three nearest neighbors separated by a shorter distance. Thus the method of distinguishing between  $sp^3$  and  $sp^2$  sites used in this work is based on determination of the coordination number of each atom.

In order to define the coordination number, the radial distribution function  $g(r)$  of the carbon structures simulated is calculated. For each atom number,  $i$ , its distance  $r_{ij}$  to an atom number  $j$  is calculated, for  $j$  running over all the atoms of the crystal. Traditionally, if this distance is in a radius restricted to the interval from  $r$  to  $r + dr$  (defined by a previously assumed parameter), the label of the atom  $j$  and its distance is stored in the list of nearest neighbors of the atom  $i$ . Afterwards the number of atoms (bonds) in each list is summed and the atom is characterized.

A new method to characterize the folding of the carbon atoms was developed in this thesis. The distance of each atom  $i$  to another  $j$  atom in the crystal is calculated. Then the distances are sorted in ascending order. This list of distances presents clear blocks corresponding to the nearest neighbors, the 2nd order neighbors, etc. Then only atoms that do not present significant variations for the distances in this block are counted as part of the  $n$  neighbor.

The advantage of this method is that no previous assumptions are considered and distorted states are clearly identified. It allows precise measurement of the bond lengths and their variations. The gap for amorphous carbon appears naturally and the differences between hybridization states bond lengths are emphasized. Clearly,

this method can also be used for other types of atoms, without previous knowledge of distances.

The old and new methods were applied and compared, leading the statistical approach to improved characterizations and enhanced visualizations. The angular distribution function  $g(\theta)$  was also calculated. The angles between the atom  $i$  and each pair of its nearest neighbors are accumulated in the list of angles.

### 3.8 Periodic boundary conditions

The goal of the computer simulation is to describe the behavior of macroscopic systems that contain an order of  $10^{24}$  particles. Obviously, this cannot be done by the molecular dynamics technique with any currently envisaged computer. Consequently, placing the boundary atoms at some fixed sites will irremediably influence the atoms in the bulk after a short time, giving rise to undesired results.

One way to overcome this problem is to use periodic boundary conditions. When they are applied, a particle that crosses a face of the simulation box, is reinserted at the opposite face. The primary simulated box is then periodically replicated in all directions to form a macroscopic sample. Thus, the neighbors that surround it and the forces applied on it would be different to those in the case of fixed boundary conditions. One of the main consequences of this kind of boundary condition is that it will give rise to energy reflections from the boundaries, which can be helpful in the case of amorphous crystal simulation [16] [29].

## 3.9 Visualization

Visualization was essential for development of this project. The Computational Physics Group at the Technion developed the Atomic Visualization package AViz [30]. This is a very powerful visualization tool which helps to enhance 3D perception. It includes various options, which let one to rotate the still sample, change relative sizes of atoms, create animations and movies, add and remove the bonds and borders of the sample, use color coding, slice the sample and much more.

The Atomic Visualization package (AViz) was used extensively in all stages of this work. A visualization of our amorphous carbon samples with color coding for different atomic bonding helped identify clusters of either  $sp^2$  or  $sp^3$  coordinated atoms, rings, graphite-like planes. Many programs and techniques for increasing the power of AViz and to make easier to work with input and output files were developed. Some of these are described in [31, 32, 33, 34].

## 3.10 Plato

PLATO [35] [36] is based upon the use of short-ranged atomic like orbitals for density functional theory (DFT) calculations. The orbitals are generated by confining atoms within spheres, these orbitals are then smoothed so that the first and second derivatives go to zero at the boundary. This forms a very efficient basis set that is ideal for treating large systems within DFT.

The PLATO code was written by Steven Kenny at Loughborough University and Andrew Horsfield at UCL. PLATO was used for Molecular Dynamics and for Molecular Dynamics Tight Binding simulations. PLATO was introduced during this thesis to the Computational Physics Group at the Technion.

---

PLATO input and output files are very big and difficult to work with. The need of creating many simulations and to import and export data to the visualization program, AViz, required the development of an auxiliary machinery in order to work efficiently and to reach the desired results. Auxiliary programs were developed using C, AWK and Python. These are discussed further in Appendix A.





# Chapter 4

## Sample characterization and preparation

### 4.1 Recharacterization

Simulations of the graphitization of diamond samples have been made previously. A new characterization method was developed and applied in order to produce new visualizations of samples from a previous work of David Saada [4]. The machinery developed for this thesis was tested on these samples.

In [4] the structural modifications that a highly damaged region in diamond undergoes upon thermal annealing have been studied by molecular dynamics simulations. The Tersoff potential was used for describing the thermally driven transition of diamond to graphite by calculating the thermal graphitization of a diamond slab. In addition, diamond samples were damaged by ion implantation, creating a region of  $sp^2$  damaged carbon. The samples with these damage regions were then annealed, with molecular dynamics, at 3000K for up to 25ps. It was found that dislodged carbon

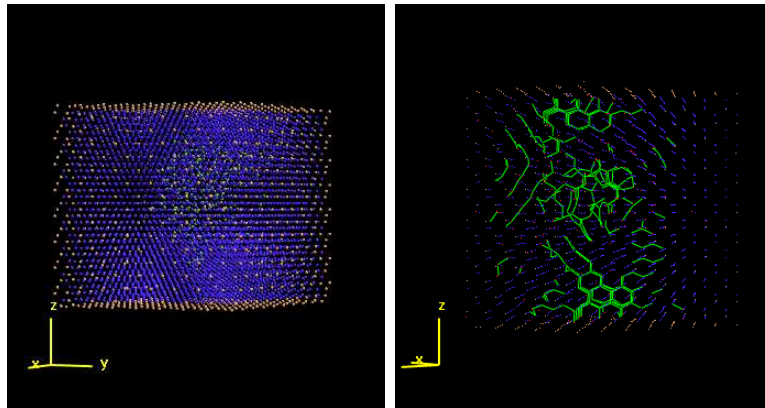


Figure 4.1: A sample of 5120 carbon atoms, in a diamond structure, after damage and after annealing. On the left the complete sample. On the right, a cut at the center where the graphitization process is clearly observed.  $sp^3$  atoms are colored in blue,  $sp^2$  atoms and bonds are colored in green. The border atoms are painted in brown.

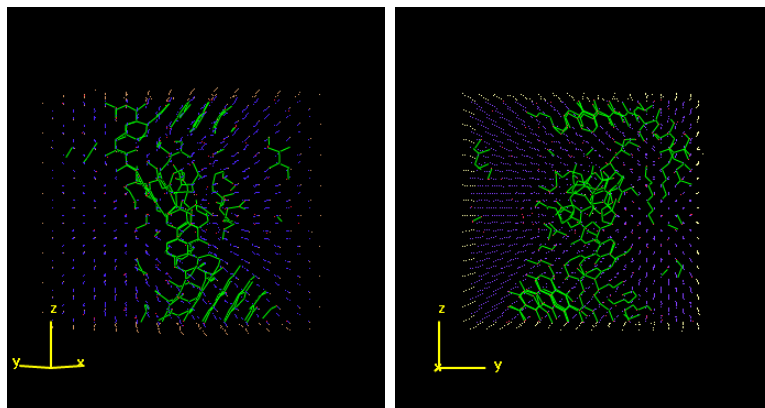


Figure 4.2: Two detailed views of the previous sample of 5120 carbon atoms. A cut of the center is shown. The graphitic planes are clearly presented.  $sp^3$  atoms are colored in blue,  $sp^2$  atoms and bonds are colored in green.

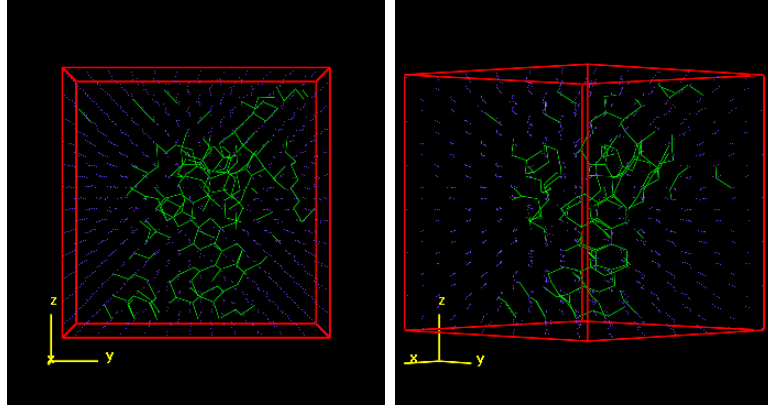


Figure 4.3: Two views of 6x6x6 unit cell, after damage and after annealing. The graphitic planes are easily appreciated. Compare with Figure 4.4.  $sp^3$  atoms are colored in blue,  $sp^2$  atoms and bonds are colored in green.

atoms in the periphery of the damaged region tended to rearrange as threefold coordinated atoms in a planar graphitic structure oriented along the  $\langle 111 \rangle$  directions of the diamond.

A damaged diamond sample composed of 5120 atoms was damaged and then annealed as seen in Figure 4.1. After the annealing we can see the graphitization process clearly. A view at the center of the sample shows off the graphitic planes in Figure 4.2.

## 4.2 Cutting the sample

In order to prepare samples for new calculations, a part of the sample presented above was taken from the original one. This was done using the Python tools. In Figure 4.3 we can see a 6x6x6 unit cell taken from the original sample that clearly present the graphitic planes. This figure can be compared with the previous picture of Saada, Figure 4.4, characterized with the classic method using cutoffs.

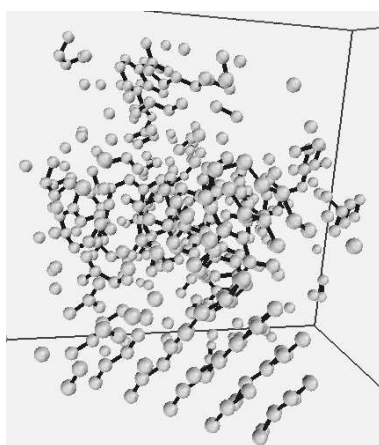


Figure 4.4: This figure is taken from the original work of Saada et al. [4]. Only threefold coordinated atoms and their nearest neighbors (if threefold) are displayed and connected by bonds. White and black spheres indicate threefold and fourfold coordinated atoms respectively. The graphitic planes are observed at the bottom of the picture.

# Chapter 5

## Results

### 5.1 Calibration samples

In order to study the differences between the different programs and techniques, and in order to select the size of the samples and evaluate the time required for the calculation, many regular samples of different carbon configurations were prepared, including samples of pure diamond, graphite and graphene, in different sizes.

#### 5.1.1 DOS, LDOS and RDF calculation in different regular samples

Many samples were created in order to study the Density of States (DOS) and Local Density of States (LDOS) of different configurations of carbon atoms in different ordered states. The first objective was to check the consistency of the results obtained from the calculations by comparing different methods and finding the optimal parameters to obtain more significant results within the limits of the available computational time and power. These results were verified with theoretical results when

such data were available. All the graphs of DOS and LDOS in this chapter have the **Energy** (eV) on the **x** axis and the **DOS** (arb. units) on the **y** axis.

### 5.1.2 Diamond

The density of states of 64 carbon atoms in a diamond configuration was calculated using two tight binding methods: orthogonal tight binding and the Frauenheim method [37, 18, 38]. We see in Figure 5.1 a good correspondence between both methods. In Figure 5.2 we explore different k-point selection methods. We observe in Figure 5.3 that the smoothness of the curve is increasing with the number of k-points used in the calculation.

Different methods for the calculation of the k-points were compared: geometrical, Monkhorst-Pack and calculation at the Special Gamma k-point were investigated. From the analysis of Figure 5.2 we can see that the results are similar for all methods when the number of k-points increases. Furthermore, increasing the quantity above 3x3x3, 27 k-points results in a much longer computational time without producing a significant increase of the result quality. In addition, an increase in the number of k-points can be used in order to reduce the number of atoms in the calculations.

For rapid prototyping, calculations at the Special Gamma k-point can be sufficient. Using either more k-points or increasing the number of atoms in the sample results in more precise results, as we can conclude from Figures 5.3 and 5.4. We can see that increasing the number of atoms in the sample over the 512 atoms does not produce significant improvement of the results in spite of the computational time that was much longer. All these results were crucial for choosing the size of further samples.

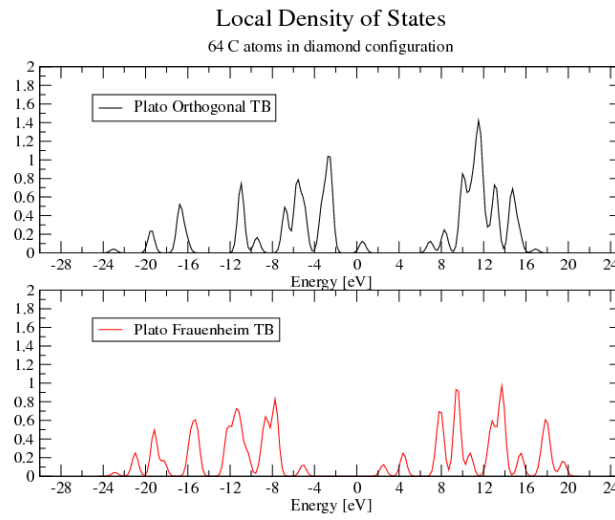


Figure 5.1: Orthogonal and Frauenheim DOS comparison.

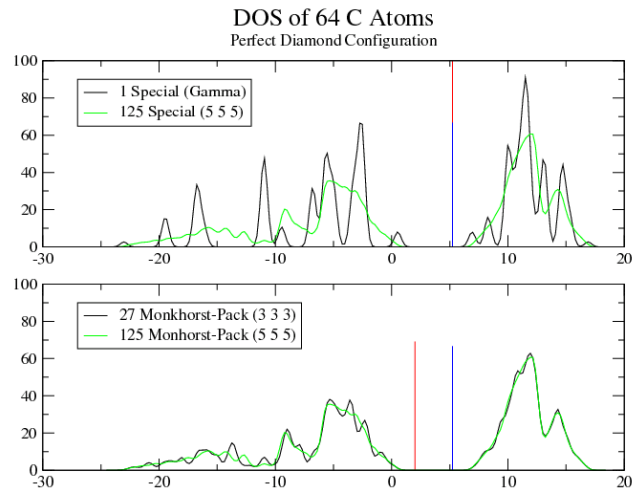


Figure 5.2: Special vs Monkhorst-Pack k-point selection.

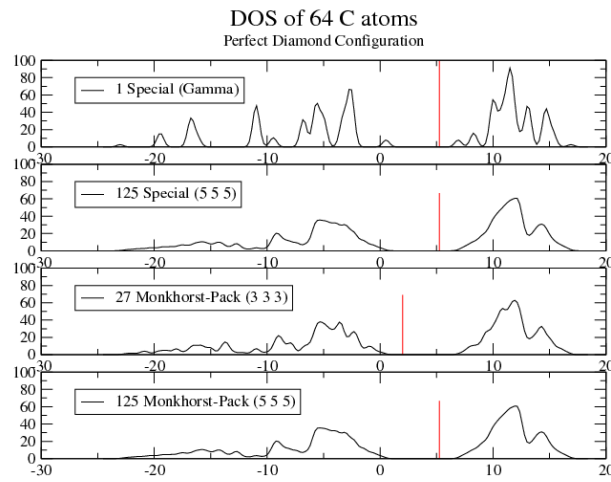


Figure 5.3: Variable number of k-points comparison.

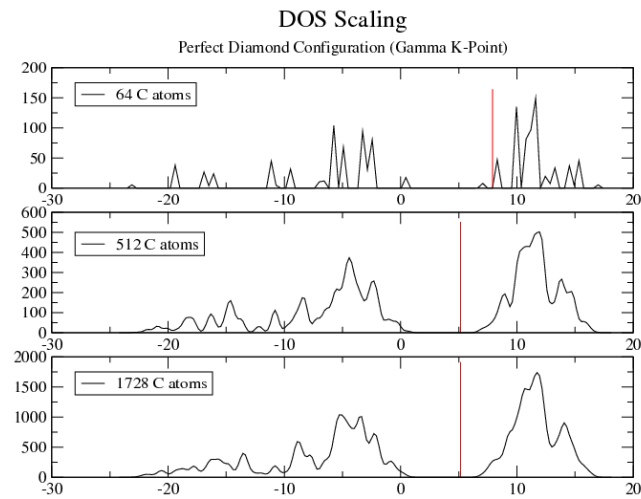


Figure 5.4: DOS scaling variation with the number of atoms.



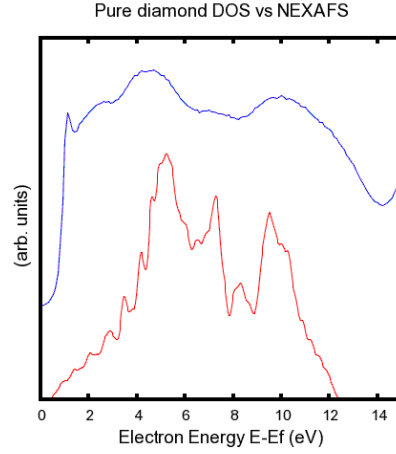


Figure 5.5: Detailed comparison between DOS calculation and NEXAFS for CVD diamond.

DOS calculations results in Figures 5.2, 5.3, 5.4 can be compared with experimental NEXAFS results for CVD diamond in Figure 5.5. [5] We can observe good qualitative agreement between them. The whole simulated sample spectrum is broader (goes further in  $E$ ) than the experimental NEXAFS.

### 5.1.3 Vacancy DOS comparison

Samples with missing atoms (vacancies) in the diamond lattice have differences in the DOS and LDOS spectra. Vacancy configurations, with a variable number of defects were calculated. A characteristic *blip* appears in the band gap of the DOS calculation, corresponding to the new energy configurations due to the vacancy. This can be seen in Figure 5.6

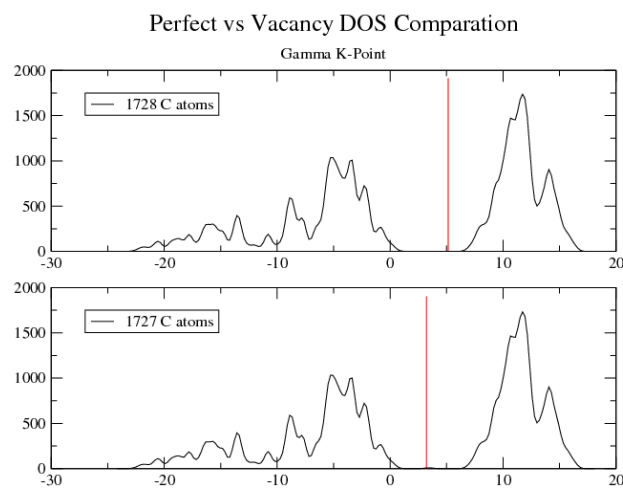


Figure 5.6: Graphs of DOS as a function of energy in eV. Upper image: perfect diamond configuration. Lower image: diamond with vacancy. The characteristic *blip* result of the free states due to the vacancy is observed in the gap at the Fermi energy (red line).

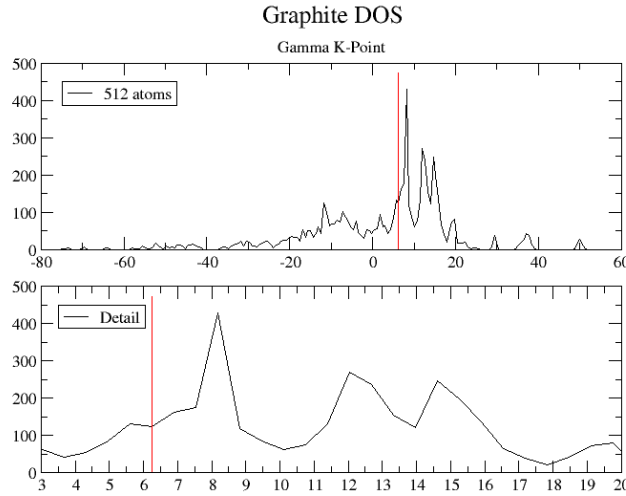


Figure 5.7: Graphite DOS calculation for 512 C atoms

#### 5.1.4 Graphite and graphene

Different sizes of graphite samples were prepared and DOS calculations were carried out. These samples were calculated only with Plato. As part of this project, Oxon results were compared and were found to be not reliable. This is another reason why Plato was chosen for this work.

DOS results for the graphite can be seen in Figure 5.7. The DOS calculation results can be compared with experimental NEXAFS [5] results for Highly Pyrolytic Graphite (HOPG) shown in Figure 5.8. We can observe good qualitative agreement between them. NEXAFS for Highly Oriented Pyrolytic Graphite, HOPG, and DOS results were compared in Fischer et al [39] and we agree with both the experimental and computational results reported therein. The simulated sample spectrum is broader (covers more values of  $E$ ) than the experimental NEXAFS.

Graphene is a single sheet of graphite. A graphene image can be seen in Figure 1.6.

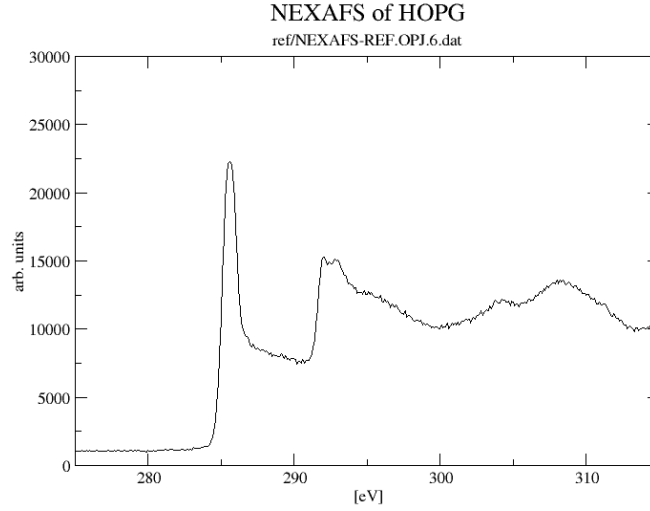


Figure 5.8: NEXAFS (arbitrary units) as a function of energy in eV for HOPG. [5]

This model was built in order to check the results of the RDF calculations. DOS calculations for 128 C atoms in one graphene sheet can be seen in Figure 5.9.

## 5.2 Amorphous carbon

One of our objectives was to simulate nano-diamond cores in a matrix of amorphous carbon. Such samples are an important step towards studying micro and nano crystalline diamond film formation by chemical vapor deposition (CVD) methods. In addition, they can play a fundamental role in the study of the hydrogen functionality in the nano-diamond formation by CVD.

Amorphous carbon structures were built in order to compare the properties of our samples with experimental NEXAFS results. The building process for the amorphous structure was carried out in two stages. An initial pure diamond sample was melted

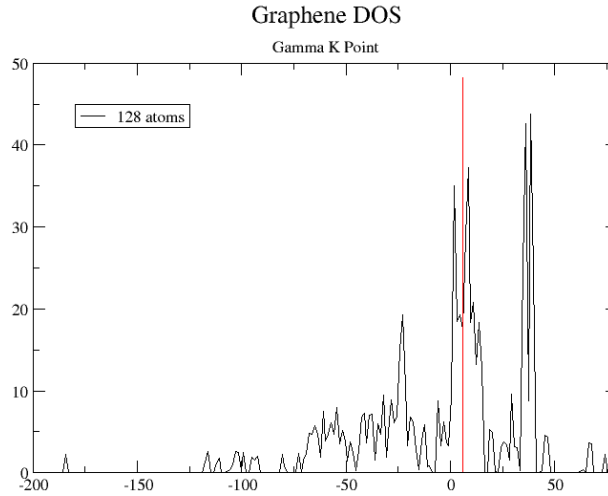


Figure 5.9: DOS for a graphene sheet.

and then quenched. Due to the long computational times needed to simulate this process, Molecular Dynamics methods with empirical potentials were used for this step. After melting the sample temperature was reduced until an equilibrium was reached. Different temperature gradients were tested for this process.

During the process, snapshots of the physical properties were calculated in order to assure the reliability of the results and plausibility of the final sample. This approach was needed in order to obtain the samples in a reasonable period of computational time. More accurate alternative methods as Local Density Approximation (LDA) and Tight Binding (TB), were considered but would have required impractically long computational times.

The second stage was to relax the equilibrated sample using Frauenheim or Orthogonal Tight Binding methods to obtain more accurate atomic configurations, as described above in 5.1.2.

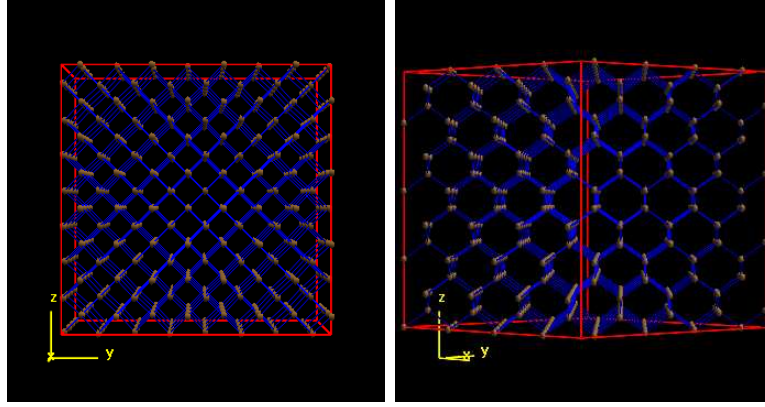


Figure 5.10: Two views of 512 carbon atoms in a perfect diamond configuration.

### 5.2.1 Amorphous carbon in the entire sample

Samples of 512 C atoms in a pure diamond configuration, as shown in Figure 5.10, calculated with periodic boundary conditions were melted using molecular dynamics in the NPT (fixed number of atoms  $N$ , pressure  $P$ , and temperature  $T$ ) ensemble. Intermediate results for the liquid phase after 5000 steps are shown in Figures 5.11, 5.12 and 5.13. Results for the liquid state of this specific sample after 10K steps in the liquidizing process are shown in Figures 5.14 and 5.15. Table 5.1 shows the hybridization status of this stage. The results are consistent with a liquid state. Further time development of the samples does not give changes to the physical properties. Many samples were made in order to reduce statistical errors. As well as averages over these cases, the individual graphs superimposed on each other will be shown. After liquidizing, the sample was cooled until it reached equilibrium conditions. After the cooling phase the model was relaxed using Tight Binding techniques in order to achieve more accurate atomic configurations.

Characterization of the samples based on the statistical coordination function can be seen in table 5.2. An example of calculus for different seeds of the ratios

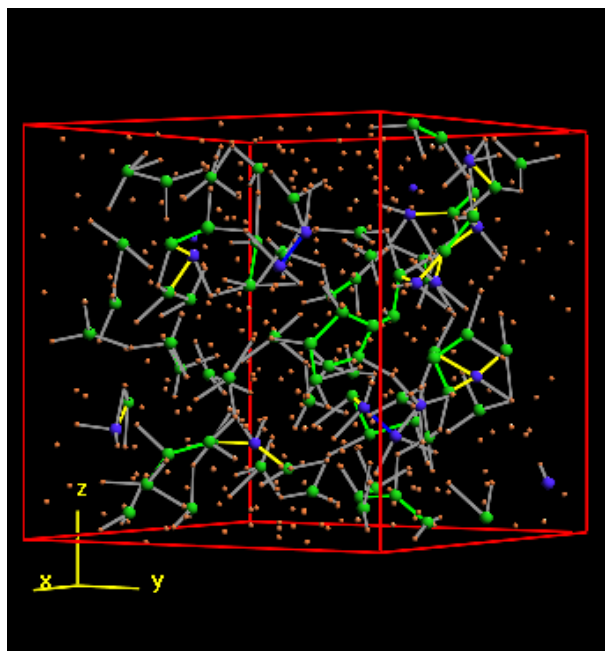


Figure 5.11: 512 carbon atoms in liquid phase after 5000 MD steps.

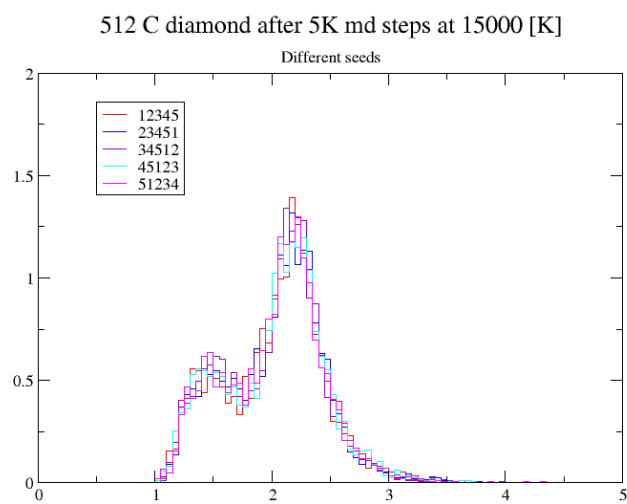


Figure 5.12: Coordination numbers of 512 carbon atoms in liquid phase after 5000 MD steps. The number indicate the initial seeds of the randomization.

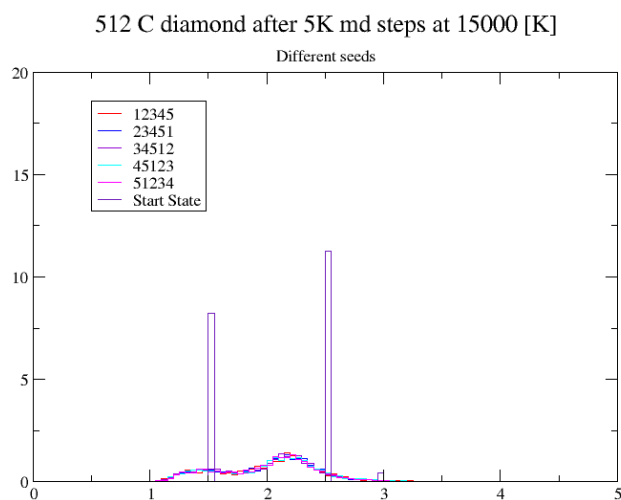


Figure 5.13: Coordination numbers of 512 carbon atoms in liquid phase superimposed to the starting state. The number indicate the initial seeds of the randomization.

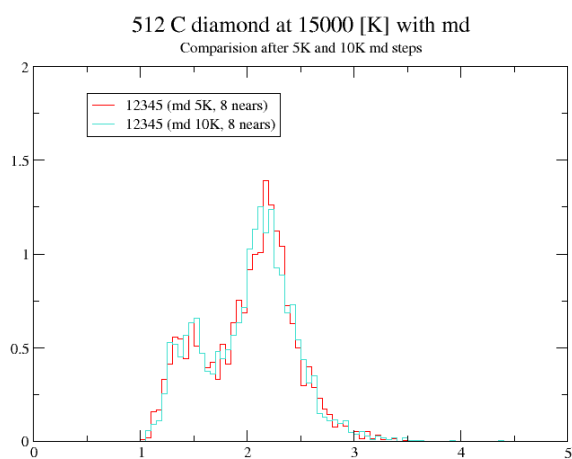


Figure 5.14: Coordination numbers of 512 carbon atoms in liquid phase after 10000 MD steps. The number indicate the initial seeds of the randomization.



Nearest neighbors		
Nearest	Atoms	Hybridization
1	219	sp2 sp3
2	211	
3	63	
4	18	
5	1	
6	0	

Table 5.1: Nearest neighbors in the liquid phase after 10K steps.

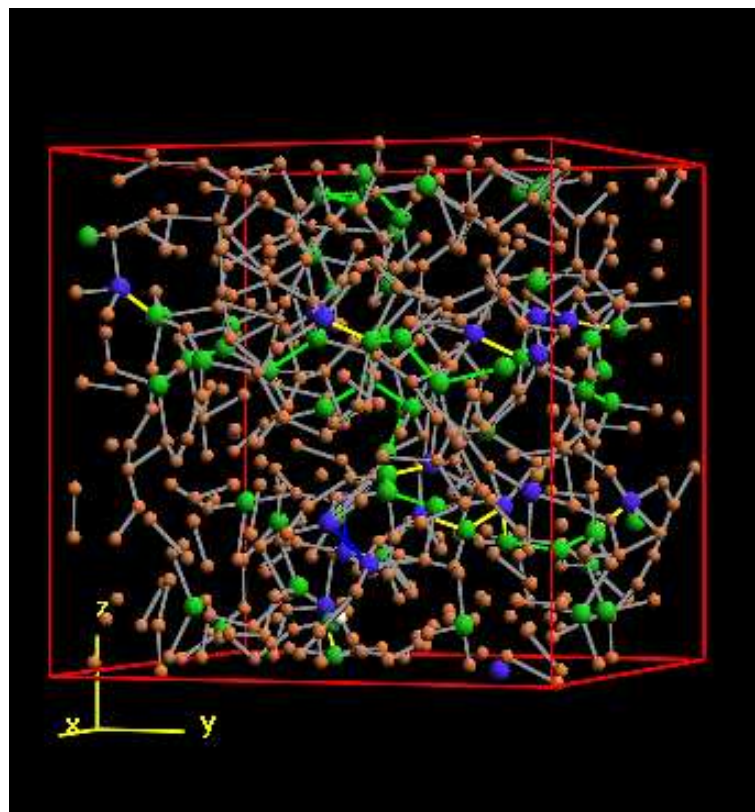


Figure 5.15: 512 carbon atoms in liquid phase after 10000 MD steps.

Nearest neighbors					
Nearest	12345	23451	34512	45123	Hybridization
1	53	48	41	51	sp2 sp3
2	132	142	121	124	
3	212	237	276	241	
4	115	85	74	96	
5	0	0	0	0	
6	0	0	0	0	

Table 5.2: Nearest neighbors for different seeds.

sp2/sp3 ratio			
Seed	sp2	sp3	ratio
12345	212	115	0.542
23451	237	85	0.359
34512	276	74	0.268
45123	241	96	0.398
51234	233	94	0.403

Table 5.3: sp2/sp3 ratio for different seeds.

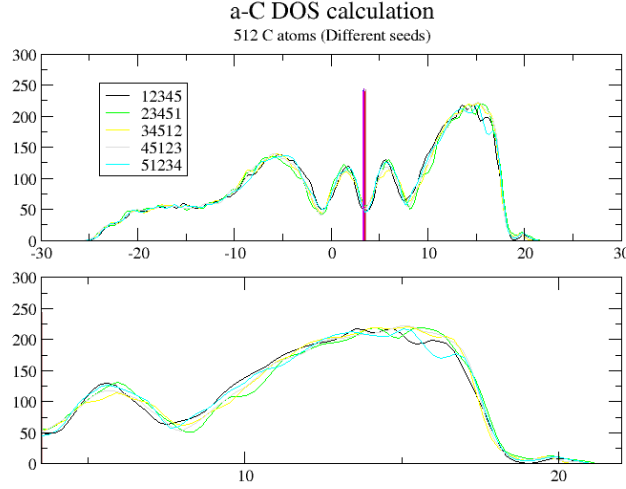


Figure 5.16: DOS calculation for a-C.

$sp^3/sp^2$  is in table 5.3. These results are in good correspondence with those in the literature [40, 41]. DOS results for the amorphous sample are in Figure 5.16 and can be compared with the results of the NEXAFS of amorphous carbon as shown in Figure 5.17. The good qualitative correspondence of all this data justify the physical coherence of the process used to build the amorphous carbon samples.

The samples were pictured using AViz during the different phases of the process to facilitate their comprehension. In Figure 5.18 is depicted the final configuration for an amorphous sample. Nano-diamond crystals can be seen where there are concentrations of  $sp^3$  atoms colored in blue. While nearest neighbor distances are as in regular carbon configurations, there is no long range order for greater distances. The characterization of the sample was done with the statistical coordination number method in order to avoid presumptions about distances and angles.

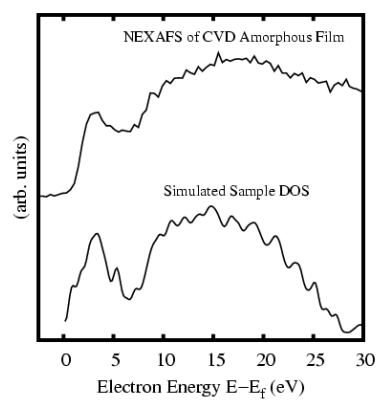


Figure 5.17: Detailed comparison between DOS calculation and NEXAFS results for amorphous carbon.

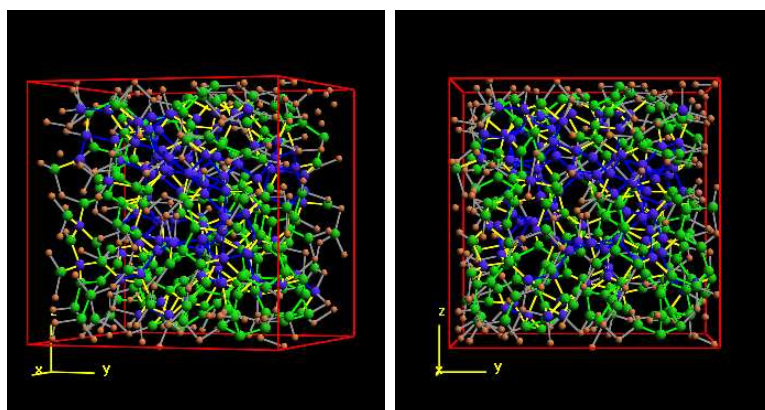


Figure 5.18: Two views of 512 carbon atoms in an amorphous configuration.

## 5.3 Mixed samples

The objective of these samples is to simulate crystalline diamond film nucleation and growth by Chemical Vapor Deposition (CVD) methods. It was experimentally observed that these films consist of nano-diamond cores embedded in amorphous carbon. Nano-diamond cores surrounded by amorphous carbon were simulated by preparing samples as in the previous section, but some of the carbon atoms were pinned in a diamond configuration during the melt and subsequent quenching process. The initial sample was equilibrated by molecular dynamics and then relaxed using Tight Binding methods.

### 5.3.1 Making an amorphous nucleus in diamond crystals

Initial samples of 512 carbon atoms in a perfect diamond configuration were melted and later quenched when some of the atoms were pinned, i.e. not allowed to move, during the simulation. Variable radius spheres of mobile atoms were melted and transformed into amorphous carbon. The outside shell of pinned atoms remained in a diamond configuration, see Figure 5.19. Carrying out the calculations with periodic boundary conditions applied to the sample, these atoms represent grains of nano-diamond inside an amorphous carbon matrix. The size of these cores was regulated with the radius of the sphere, thereby limiting the quantity of atoms it included.

The state after quenching and relaxation can be observed in Figure 5.20. Diamond like atoms are colored in blue, and the bonded atoms are in the amorphous part. Blue bonds are sp<sup>3</sup> bonds, green bonds are sp<sup>2</sup> and yellow bonds represent bonds between atoms in different (mixed) hybridized states.

Table 5.4 shows the hybridization states for the whole sample and compared to

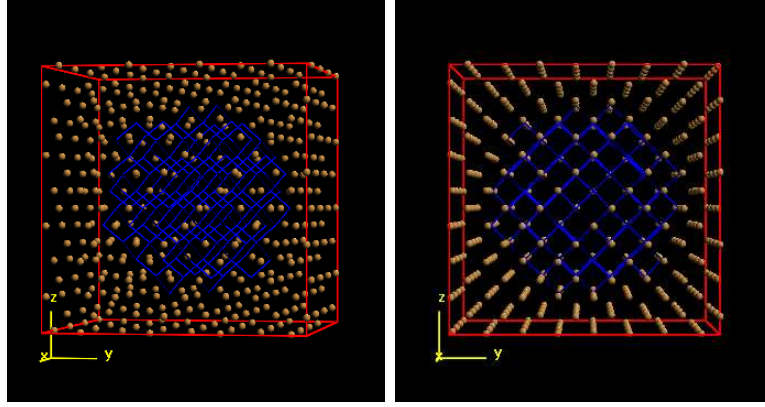


Figure 5.19: Two views of sample preparation of an amorphous sphere embedded in a diamond matrix. 512 carbon atoms still in the original diamond configuration. The bonded atoms in blue are mobile. The other are pinned.

the previous state as perfect diamond. In Table 5.5 we can see the hybridization state of the atoms only inside the sphere, standing out the amorphous state of such atoms. DOS and LDOS for different atoms calculations were carried out and are shown in Figure 5.21. All the calculations were carried many times in order to reduce statistical errors. The results of different samples are very consistent, as shown in Figure 5.22 for five different samples.

### 5.3.2 DOS comparisons

DOS calculations for all the samples were compared. Diamond, amorphous carbon, and mixed sampled DOS were plotted together in Figure 5.23. The mixed sample presents combined characteristics of the diamond and amorphous carbon sample.

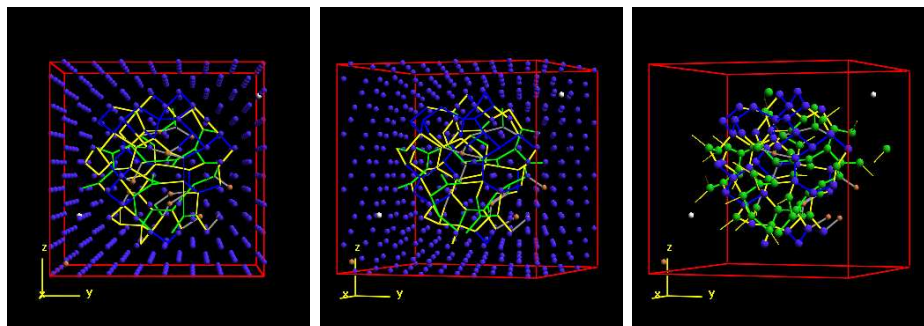


Figure 5.20: Three views of 512 carbon atoms after liquidizing and quenching a centered sphere. All the atoms displayed in left and center pictures. Not bonded atoms are pinned. In the right picture only mobile atoms are displayed.

Nearest neighbors for different seeds and regular diamond						
Nearest	12345	23451	34512	45123	Diamond 512	Hybridization
1	27	26	25	22	22	sp2 sp3
2	148	162	150	155	147	
3	74	53	85	59	0	
4	248	259	230	265	343	
5	14	9	21	10	0	
6	1	3	1	1	0	
7	0	0	0	0	0	
8	0	0	0	0	0	

Table 5.4: Hybridization states in the sample for the melted-quenched sphere sample.

Nearest neighbors in the sphere only (seed 12345)		
Nearest	Atoms	Hybridization
1	3	sp2 sp3
2	8	
3	56	
4	45	
5	1	
6	1	
7	0	
8	0	

Table 5.5: Hybridization number of the atoms inside the amorphous sphere.

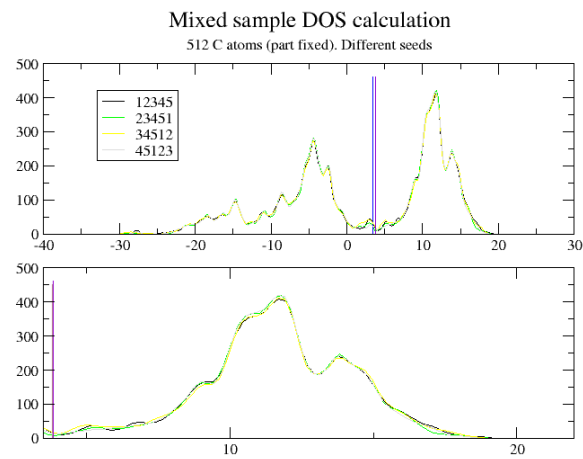


Figure 5.21: DOS of a-C sphere in a diamond.



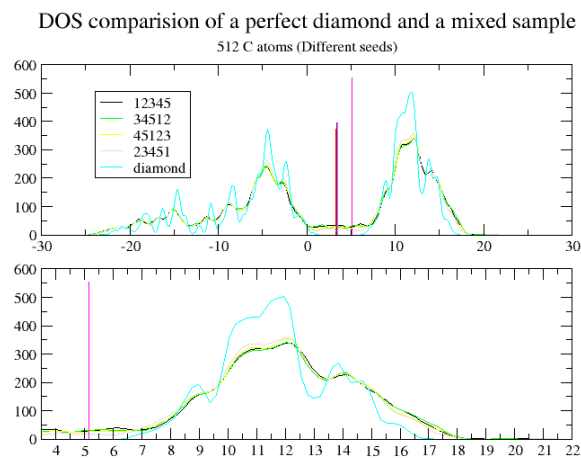


Figure 5.22: Diamond and various mixed samples comparison

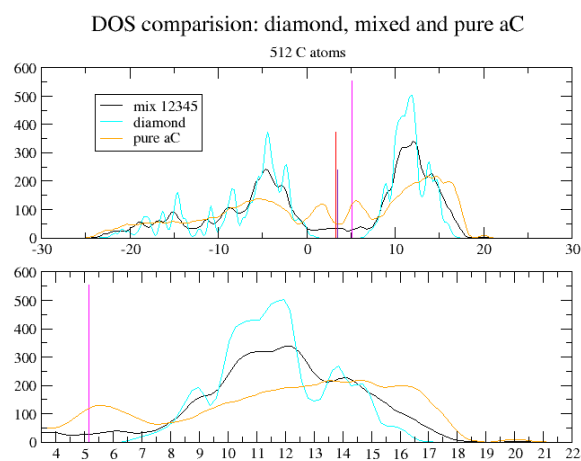


Figure 5.23: Diamond, mixed and a-C DOS comparison

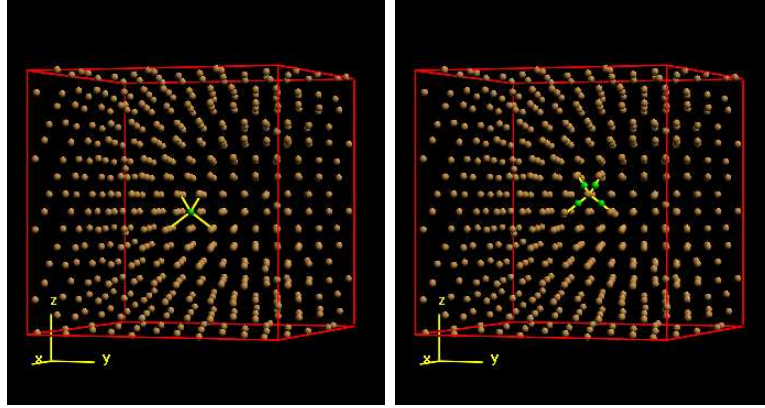


Figure 5.24: Hydrogen caged in 512 carbon atoms in a Diamond configuration. On the left, a sample with one hydrogen atom. A sample with four hydrogen atoms is shown in the right picture. Hydrogen atoms are painted in green.

## 5.4 Hydrogen in diamond

Hydrogen is an essential component of the gas mixture used for nano-diamond film nucleation growth by Chemical Vapor Deposition (CVD). The role of the hydrogen in the formation of such films has been extensively investigated. Diamond films formed by diamond cores embedded in amorphous carbon matrix created by CVD show high hydrogen retention properties. As an initial step in the study of such films, Hydrogen atoms were added to a diamond sample and DOS and LDOS calculated. Two samples were prepared: one with a single centered Hydrogen atom and another with four hydrogen atoms. See in Figure 5.24 DOS for the sample with four atoms. LDOS for regular and hydrogenated Carbon atoms is shown in Figure 5.25. A comparison between the DOS results for the two types of hydrogenated samples is shown in Figure 5.26.

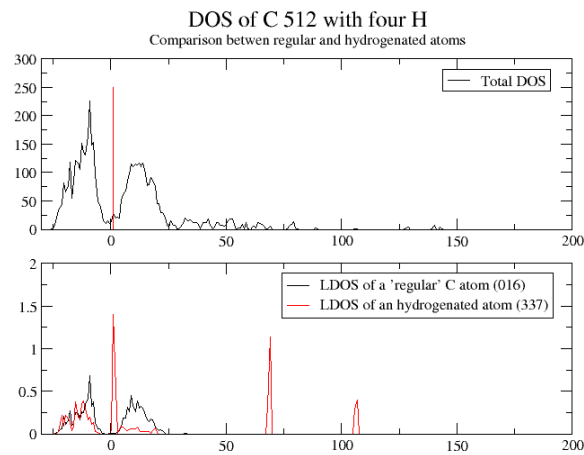


Figure 5.25: DOS calculation for a Diamond with an H atom and LDOS for regular and hydrogenated atoms.

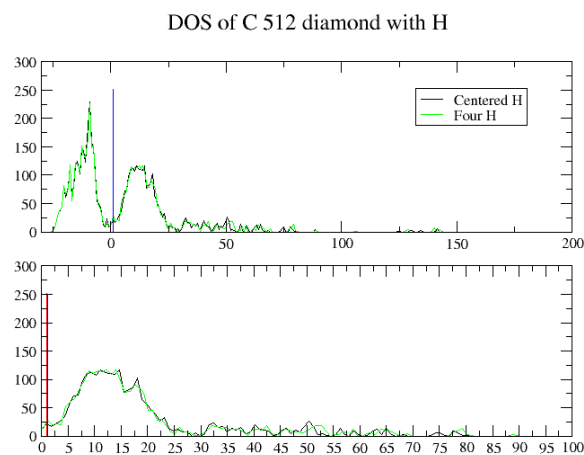


Figure 5.26: DOS comparison between one and four hydrogen atoms.



# Chapter 6

## Discussion and summary

A new characterization method for hybridization states of carbon was developed. This method is based on statistical analysis of distances and angles and makes no **a priori** assumptions of these values. The method is more accurate than using cut off values and leads to new insights of samples comprehension and improved visualization. The visualization of older samples was improved using the new method.

New programs, making possible more accurate calculations and bigger samples were developed and introduced. Many auxiliary tools were developed in order to build better simulations and to make deepen analysis of the new results. Bigger samples and extended simulations were studied, beyond the limits of previous techniques and programs used in the Computational Physics group. These developments make possible to start a new type of simulations and computational physics studies.

A new type of sample, the *mixed sample*, was created in order to make possible the studies of new phenomena, as the Chemical Vapor Deposition growing of nano-diamond films as done in the Technion. Practical ways to build and study this type of sample were developed.

Visualization techniques using AViz were improved using more features of the program and developed auxiliary tools to make the most of the AViz program. These techniques were applied also in other projects of the group.

From the results is evident the connection between our Tight Binding simulation DOS calculations and the NEXAFS results. In addition, the results from Radial Distribution Functions calculated from the samples, and the hybridization states ratio obtained, give an indication that our models for amorphous and mixed samples have physical sense. Mixed samples results compared to experimental data justify the construction method used to simulate the cores of diamond embbeded in amorphous carbon.

From the comparison of the DOS plots and NEXAFS plots we can see that all the main characteristics are common, with good qualitative agreement between calculation and experimental results. Thus we can rest assured that the relation between NEXAFS and the DOS calculations produced by Tight Binding molecular dynamics was validated. Some initial steps in to the study of samples with added hydrogen atoms were also made successfully.

# Appendix A

## Programming techniques

Many programs in C, AWK and Python were developed during this work. OXON use was discarded due to the need of bigger samples and more precise calculations. Parallel PLATO was tested.

The need to run long calculations with complex models required a lot of auxiliary programs in order to make it possible. There were many input files to prepare and many output files to analyze. In addition it was necessary to convert files between AViz and PLATO. An object oriented library that can run interactively in the Python interpreter was developed in order to make possible the creation and manipulation of the complex samples used in the research. As an example, the base class representing an atom is presented below. The complete code can be found in the companion CD.

## DESCRIPTION

```
#####
#Handles xyz files.
#
# EJW
#
#The input xyz scale is assumed in Angstroms
#####
```

## CLASSES

```
exceptions.Exception
```

```
    XyzError
```

```
        DataPointError
```

```
DataPoint
```

```
Xyz
```

```
class DataPoint
```

```
    | A datapoint. x, y, z coords and atom type
```

```
    |
```

```
    | Methods defined here:
```

```
    |
```

```
    | __init__(self, *args)
```

```
    |     Instanciates the datapoint.
```

```
    |
```

```
    |     Dispatcher.
```

```
    |     Input: A string, a tuple or four separate positional arguments,
```

```
    |     The order is: atomType, x, y, z in all cases.
```



---

```
|
|  __str__(self)
|      Datapoint as a string
|
|  asComponents(self)
|      The Datapoint as 4 separated variables
|
|      An accessor function
|
|  fromString(self, line)
|      Instanciates the datapoint from a string.
|
|  fromValues(self, atomType, x, y, z)
|      Instanciates the datapoint from separated values.
|
|  reducedCoords(self, cellLenX, cellLenY, cellLenZ, offX=0, offY=0,
|                  offZ=0)
|      Returns dp in reduced coordinates in terms of cellLenght and
|      offset.
|
|      Input:CellLenghts is a tuple (lenght x, lenght y, lenght z)
|
|  translateTo(self, newOrig)
|      Returns a new DataPoint with coords translated to newOrig.
|
```

```

|         Input: the new origin of coordinates.
class DataPointError(XyzError)
|     Method resolution order:
|         DataPointError
|         XyzError
|         exceptions.Exception
|
|     Methods inherited from exceptions.Exception:
|
|     __getitem__(...)
|
|     __init__(...)
|
|     __str__(...)
class Xyz
|     xyz class
|
|     Methods defined here:
|
|     __add__(self, other)
|
|         Returns a new Xyz composed by all the dp's of self and other.
|
|     __init__(self, data, comment='')
|
|         Instance a new Xyz file from a file, or a list of strings or
|         DataPoints.

```

```
|  
|     Dispatcher for fromList or fromFileName  
|  
|     __str__(self)  
|  
|     cellSize(self)  
|         Returns the size of the cell  
|  
|     cut(self, func, invert=False, *args)  
|         Returns an Xyz class object with the datapoints for they  
|         func(dp) is true.  
|  
|         Input:  
|         func: Boolean function on a datapoint (e.g. prism())  
|         *args: the arguments for this function.  
|  
|         Use invert = True if you want to complement (invert) func()  
|         output.  
|         i.e. the points outside the prism.  
|  
|         Output:  
|         Xyz class object.  
|  
|     fromFileName(self, filename, comment)  
|         Reads a xyz file and makes the object.
```

```
|
|
|     Input: filename (string)
|
|
| fromList(self, dpList, comment='')
|
|     Makes a Xyz object from a list of datapoints.
|
|
|     The number of datapoints is the len of the list.
|
|     Input can be a list of string or datapoints.
|
|     Will work with non-homogeneous lists, but avoid this.
|
|
| maximum(self)
|
|     Returns the minimum of x, y, z
|
|
| minimum(self)
|
|     Returns the minimum of x, y, z
|
|
| prism(self, dp, dp0, dp1)
|
|     Return True if dp is inside the prism defined by dp0, dp1.
|
|
|     Input:
|
|     dp0: lower diagonal point
|
|     dp1: upper diagonal point
|
|
| toPlatoIn(self, format=0)
|
|     Produces a string in Plato .in representing the xyz
```

---

```
|
|
|     (from plato .in file)
|
|     format determines the input format for atomic coordinates.
|
|     0 ==> Reduced coordinate format in units of the
|
|             translation vectors
|
|     1 ==> z-matrix format
|
|     2 ==> (x,y,z) format in units of the lattice constant
|
|
| translateTo(self, newOrig)
|
|     Returns a new XYZ with each datapoint coords moved by dp.
|
|
|     Input: newOrig is an aux DataPoint representing a new coords
|
|            origin.
|
|     Output: a new XYZ instance.
|
|     No changes the original XYZ
class XYZError(Exception)
|
|     Base error class in xyz files.
|
|
|     Methods inherited from Exception:
|
|
|     __getitem__(...)
|
|
|     __init__(...)
|
|
|     __str__(...)
```



# References

- [1] F. P. Bundy. Pressure-temperature phase diagram of elemental carbon. *Physica A*, 156:169–178, 1989.
- [2] H. Ade. <http://www.physics.ncsu.edu/stxm/nexafs.html>.
- [3] A. Chaiken. <http://en.wikipedia.org/wiki/File:Photoabsorb.png>. Using xfig.
- [4] David Saada, Joan Adler, and R. Kalish. Computer simulation of damage in diamond due to ion impact and its annealing. *Phys. Rev. B*, 59(10):6650–6660, 1999.
- [5] A Hoffman and A Laikhtman. Photon stimulated desorption of hydrogen from diamond surfaces via core-level excitations: fundamental processes and applications to surface studies. *J. Phys.: Condens. Matter*, 18(30):S1517–S1546, 2006.
- [6] W. D. Callister. *Material Science and Engineering*. John Wiley and Sons, 2002.
- [7] S. Iijima. Helical microtubules of graphitic carbon. *Nature*, 354:56–58, 1991.

- 
- [8] L. Pauling. *The nature of the chemical bond*. Cornell University Press, 1948.
- [9] M.J. Sienko and R.A. Plane. *Chemistry: Principles and Applications*. McGraw-Hill, 1979.
- [10] J. Stohr. *NEXAFS Spectroscopy*. Springer, 1996.
- [11] I. Gouzman, I. Lior, and A. Hoffman. Formation of the precursor for diamond growth by [bold in situ] direct current glow discharge pretreatment. *Applied Physics Letters*, 72(3):296–298, 1998.
- [12] Y. Lifshitz, Th. Kohler, Th. Frauenheim, I. Guzmán, A. Hoffman, R. Q. Zhang, X. T. Zhou, and S. T. Lee. The Mechanism of Diamond Nucleation from Energetic Species. *Science*, 297(5586):1531–1533, 2002.
- [13] S. T. Lee, H. Y. Peng, X. T. Zhou, N. Wang, C. S. Lee, I. Bello, and Y. Lifshitz. A Nucleation Site and Mechanism Leading to Epitaxial Growth of Diamond Films. *Science*, 287(5450):104–106, 2000.
- [14] D.J. Chadi and M.L. Cohen. Tight-binding calculations of the valence bands of diamond and zincblende crystals. *Phys.Stat.Solida B*, 68:405–419, 1975.
- [15] Per-Olov Löwdin. On the non-orthogonality problem connected with the use of atomic wave functions in the theory of molecules and crystals. *The Journal of Chemical Physics*, 18(3):365–375, 1950.
- [16] J. Tersoff. Empirical interatomic potential for carbon, with applications to amorphous carbon. *Phys. Rev. Lett.*, 61(25):2879–2882, 1988.



- 
- [17] Thomas A. Weber and Frank H. Stillinger. Local order and structural transitions in amorphous metal-metalloid alloys. *Phys. Rev. B*, 31(4):1954–1963, 1985.
- [18] L. Colombo. Tight binding molecular dynamics simulations. *Computational Materials Science*, 12:278, 1998.
- [19] M. Born and J.R. Oppenheimer. Zur quantentheorie der molekeln. *Ann. Phys.*, 84:457, 1927.
- [20] J. C. Slater and G. F. Koster. Simplified lcao method for the periodic potential problem. *Phys. Rev.*, 94(6):1498–1524, 1954.
- [21] S. Fahy and Steven G. Louie. High-pressure structural and electronic properties of carbon. *Phys. Rev. B*, 36(6):3373–3385, 1987.
- [22] L. Goodwin, A. J. Skinner, and D. G. Pettifor. Generating transferable tight-binding parameters: Application to silicon. *EPL (Europhysics Letters)*, 9(7):701–706, 1989.
- [23] C H Xu, C Z Wang, C T Chan, and K M Ho. A transferable tight-binding potential for carbon. *Journal of Physics: Condensed Matter*, 4(28):6047–6054, 1992.
- [24] R. P. Feynman. Forces in molecules. *Phys. Rev.*, 56(4):340–343, 1939.
- [25] Nicholas Metropolis, Arianna W. Rosenbluth, Marshall N. Rosenbluth, Augusta H. Teller, and Edward Teller. Equation of state calculations by fast computing machines. *The Journal of Chemical Physics*, 21(6):1087–1092, 1953.

- 
- [26] Adrian P. Sutton. *Electronic Structure of Materials*. Oxford Science Publications, 1993.
- [27] Hendrik J. Monkhorst and James D. Pack. Special points for brillouin-zone integrations. *Phys. Rev. B*, 13(12):5188–5192, 1976.
- [28] D. J. Chadi and M. L. Cohen. Analytic expression for the electronic charge density distribution in diamond-structure crystals. *Phys.Stat.Solidi B*, 62:235–248, 1974.
- [29] P. C. Kelires. Structural properties and energetics of amorphous forms of carbon. *Phys. Rev. B*, 47(4):1829–1839, 1993.
- [30] J. Adler, A. Hashibon, N. Schreiber, A. Sorkin, S. Sorkin, and G. Wagner. Visualization of md and mc simulations for atomistic modeling. *Computer Phys. Communications*, 147:665–669, 2002.
- [31] J. Adler, J. Fox, R. Kalish, T. Mutat, A. Sorkin, and E. Warszawski. The essential role of visualization for modeling nanotubes and nanodiamond. *Computer Physics Communications*, 177:19, 2007.
- [32] E. Warszawski, A. Hoffman, A. Silverman, and J. Adler. *Bulletin of the Israel Physical Society*, 52:38, 2006.
- [33] J. Adler, Y. Gershon, R. Kalish, T. Mutat, A. Sorkin, and E. Warszawski. Nanodiamond and nanotubes: Visualization with aviz. *Recent Developments in Computer Simulation Studies in Condensed Matter Physics edited by D. Landau, S. P. Lewis and B. Schuttler*, XVII:56–60, 2009.

- 
- [34] E. Warszawski, A. Silverman, A. Hoffman, and J. Adler. *Recent Developments in Computer Simulation Studies in Condensed Matter Physics* edited by D. Landau, S. P. Lewis and B. Schuttler, XX:submitted, 2009.
- [35] Andrew P. Horsfield. Efficient ab initio tight binding. *Phys. Rev. B*, 56(11):6594–6602, 1997.
- [36] S. D. Kenny, A. P. Horsfield, and Hideaki Fujitani. Transferable atomic-type orbital basis sets for solids. *Phys. Rev. B*, 62(8):4899–4905, 2000.
- [37] L. Colombo. Tight-binding molecular dynamics. *Annual reviews of Computational Physics*, IV:147, 1996.
- [38] M. Elstner, D. Porezag, G. Jungnickel, J. Elsner, M. Haugk, Th. Frauenheim, S. Suhai, and G. Seifert. Self-consistent-charge density-functional tight-binding method for simulations of complex materials properties. *Phys. Rev. B*, 58(11):7260–7268, 1998.
- [39] D. A. Fischer, R. M. Wentzcovitch, R. G. Carr, A. Continenza, and A. J. Freeman. Graphitic interlayer states: A carbon k near-edge x-ray-absorption fine-structure study. *Phys. Rev. B*, 44(3):1427–1429, 1991.
- [40] H.O. Pierson. *Handbook of carbon, graphite, diamond and fullerenes*. Noyes Publications, 1993.
- [41] D. G. McCulloch, S. Prawer, and A. Hoffman. Structural investigation of xenon-ion-beam-irradiated glassy carbon. *Phys. Rev. B*, 50(9):5905–5917, 1994.

**חִישׁוּבֵי צְפִיפּוֹת מַצְבִּים לַמְבֻנִים  
וְתַעֲרׁוּבוֹת שֶׁל פַּחֲמָן**

**אֲדוֹאָרְדּוֹ וִרְשֶׁבֶסְקִי**



# **חישובי צפיפות מצבים למבנים ותערובות של פחמן**

חיבור על מחקר

לשם מילוי חלקי של הדרישות לקבלת תואר  
מגיסטר למדעים  
בפיסיקה

**אדוארדו ורשבסקי**

הוגש לסנט הטכניון — מכון טכנולוגי לישראל

דצמבר 2008

חיפה

טבת תשס"ט



המחקר נעשה בהדרכת דר' יוחנה אדלר ופרופ' אלון הופמן  
בפקולטה פיסיקה

## הכרת תודה

אני מודה לטכניון על התמיכה הכספית הנדיבה בהשתלמותי





# תוכן עניינים

xv	תקציר באנגלית
1	1 מבוא
1	1.1 מבנים פחמניים שונים
4	1.2 יהלום
5	1.3 גרפיט
7	1.4 גרפין
7	1.5 פחמן אמורפי
9	1.6 מתרות המחקר
11	2 שיטות ניסיוניות
11	2.1 NEXAFS
13	2.1.1 תיאוריה
15	2.2 היווצרות גרעיני יהלום עם מימן
19	3 שיטות סימולציה
19	3.1 Ab-initio
19	3.2 חישובי LCAO
22	3.3 דינמיקה מולקולרית

22	פוטנציאלים סמי-אמפיריים	3.3.1
23	דינמיקה מולקולרית בשיטת Tight binding	3.3.2
24	מודל ה-Tight-Binding	3.3.3
27	חישובי אנרגיה	3.3.4
28	פונקציות ה-Rescaling	3.3.5
29	שלבי הסימולציה	3.3.6
30	Annealing ו-quenching	3.4
32	צפיפות מצבי אנרגיה	3.5
33	דגימת נקודות k	3.6
34	מספר הקורדינציה	3.7
35	תנאי שפה מחזוריים	3.8
36	הדמייה	3.9
36	Plato	3.10
<b>39</b>	<b>איפיון מבנה הפחמן</b>	<b>4</b>
39	אפיון מחודש	4.1
41	חיתוכי - הדגם	4.2
<b>43</b>	<b>תוצאות</b>	<b>5</b>
43	כיול	5.1
43	חישובי LDOS, DOS ו-RDF בדגמים מושלמים	5.1.1
44	יהלום	5.1.2
47	צפיפות מצבי אנרגיה של העדרות ביהלום	5.1.3
49	גרפיט וגרפין	5.1.4
50	פחמן אמורפי	5.2
52	פחמן אמורפי טהור	5.2.1

59	.....	דגמים מעורבים	5.3
59	.....	יצירת גרעינים אמורפים בגבישים יהלומיים	5.3.1
60	.....	השוואות של צפיפות מצבי אנרגיה	5.3.2
64	.....	מימן ביהלום	5.4

67		מסקנות וסיכום	6
----	--	---------------	---

69		א' טכניקות תכנות	
----	--	------------------	--

76		רשימת מקורות	
----	--	--------------	--

ט		תקציר	
---	--	-------	--



## תקציר

הפחמן נפוץ מאוד בטבע ונמצא בשמש, כוכבים, כוכבי שביט ובאטמוספירה של רוב הפלנטות. על פני כדור הארץ הפחמן הוא יסוד הבנייה של היצורים החיים. הפחמן מופיע בשלוש צורות נפוצות: יהלומית, גרפיטית ואמורפית. לכל צורה מאפיינים פיסיקליים וכימיים שונים מאוד. למשל, הגרפיט רך, אטום ומוליך חשמלית בניגוד ליהלום שהינו קשיח מאוד, שקוף ומבודד חשמלית. השוני בין הצורות הוא שהופך את הפחמן ליסוד מרתק ומעניין.

ביהלום כל אטום של פחמן קשור לארבעה שכנים קרובים ע"י קשרי  $sp^3$ , במבנה טטרהדרלי קשית. אמנם, המבנה היציב תרמודינמי של פחמן בתנאים רגילים של טמפרטורה ולחץ הוא הגרפיט, אשר בנוי ממישורים של אטומי פחמן עם שלושה שכנים קרובים כל אחד. קשרים אלה הם מסוג  $sp^2$ . בקשרי  $sp^2$  אלקטרונים הנותרים ללא קשר תורמים להולכה חשמלית. לכן סוג הקשר,  $sp^2$  או  $sp^3$ , מאפיין במידה רבה את התכונות האלקטרוניות והפיסיקליות של צורות אלה של פחמן ומהווה בעיית מפתח בהבנת התנהגות מבנה היהלום בזמן גידול גבישים.

במעבדות רבות בעולם נערך מחקר רחב הקף על גידול יהלומים. גידול יהלומים וננו-יהלומים הוא בעל חשיבות טכנולוגית מהמעלה הראשונה עקב המאפיינים המיוחדים שלהם והיכולת האפליקטיבית בתחומים רבים כגון ציפויים קונפורמליים למערכות מיקרואלקטרוניות, אלקטרודות אלקטרוכימיות לתאי דלק ומשטחים פולטי אלקטרונים

למסכים שטוחים. גידול ננו־גבישים פחמניים בעלי אופי יהלומי נערך בשיטת ה־Chemical Vapor Deposition בסביבת פלסמה. מחקרים מצביעים על קשר הדוק בין טמפרטורת הגידול ומרכיבי הפלסמה לכמות ולגודל גבישי הננו־הלום הנוצרים. במעבדה נמצא כי הגידול המירבי הושג בטמפרטורה של  $880^{\circ}\text{C}$  מעלות מתוך 9% מתאן ו־91% מימן. ריכוזים שונים של הגזים או טמפרטורות שונות הביאו לירידה בכמות הננו־הלום. בנוסף, כאשר הוחלף גז המימן בגז אציל אחר כמו ארגון, שוב התקבלה ירידה בכמות הננו־הלום. לפיכך אפשר לשאול מהי תרומת המימן לגידול הננו־הלום ומהו הריכוז האופטימלי של המימן בגביש.

קיימים כמה מודלים לתאר את האינטרקציה בין אטומים והתנועה הדינמית שלהם. המודל הכי מדויק הוא מודל ה־ab-initio אשר מבוסס על תאורית פונקציונל הצפיפות. במודל זה משתמשים לעתים קרובות בקירוב הצפיפות הלוקלית וניתן לשנותו בעזרת תיקון בגרדיאנט הצפיפות. ברוב המחקרים שנעשים כעת עם מודל ה־ab-initio, גלים מישוריים מהווים בסיס לפונקצית הגל האלקטרונית, ופסוידופוטנציאלים מתארים את האינטרקציה בין אלקטרוני ערכיות לבין הליבה היונית. מתייחסים לאטומים כאל קלאסיים ופותרים את משוואות Newton בכדי לקבל את מיקומם ואת מהירותם של האטומים כפונקציה של הזמן.

המודל השני, שגם הוא בשימוש רחב, נקרא מודל ה־Tight-Binding. במודל זה משתמשים בבסיס מצומצם של ארבעה אורביטלים במקרה של יהלום, ופונקציונל אמפירי מתאר את החלק הדוחה של האינטרקציה הבין אטומית. המודל הזה פחות מדויק מהקודם אבל דורש פחות כוח חישוב. יתרון נוסף לשיטה זו הוא שניתן בעזרתה לחשב את רמות האנרגיות של הדגם שנוצר בסימולציה.

מבנים פחמניים שונים סומלצו על מנת להבין בצורה מעמיקה יותר תהליכים ותכונות של ננו־הלומים בשכבות דקות. תוצאות הסימולציה הושוו לתוצאות ניסיוניות של NEXAFS. הסימולציות כללו מאות ואלפי אטומים ע"י חישובים בשיטת Tight-Binding.

הובחן בצורה ניסיונית, שגידול של ננו־הלומים ע"י Chemical Vapor Deposition בתנאים של פלסמה עשיר בפחמימנים, מורכב מגרעינים של ננו־הלומים טבולים בפחמן אמורפי. סימולציות של מיבנים כאלו נחוצים על מנת להבין בצורה מעמיקה וטובה יותר תהליכי גידול ותכונות של ננו־הלומים.

לצורך מחקר זה פותחו שיטות חישוב חדשות ותוכנות חיוניות לקבלת התוצאות המוצגות. פותחה שיטה חדשה לאפיון של מצבי היברדיזציה של אטומי פחמן. שיטה זו מבוססת על ניתוח סטטיסטי של מרחקים וזוויות ואינה מניחה מראש דבר לגבי ערכים אלו. שיטה זו מדויקת יותר מאשר שימוש בערכי המרחקים הידועים מראש ומובילה לתובנות חדשות ועמוקות יותר בהבנת מבנים פחמניים ולויזואליזציות משופרות. ויזואליזציות חדשות של מבנים ישנים הראו שיפורים דרסטיים לטובה.

תוכנות חדשות המאפשרות חישובים מדויקים יותר והתמודדות עם מודלים גדולים יותר פותחו והוכנסו לשימוש במהלך עבודה זו. כלי עזר רבים פותחו בכדי לשפר את איכות הסימולציות ולהשגת הבנה עמוקה יותר של התהליכים הפיזיקאליים. סימולציות עם מספר רב יותר של אטומים ולאורך זמנים ארוכים יותר נותחו, מעבר למגבלות של טכניקות ותוכנות קודמות בשימוש בקבוצת הפיזיקה החשובית בטכניון. עבודה זו אפשרה את התפתחותם של זן חדש של סימולציות, חישובים ומחקרים בקבוצת הפיזיקה החשובית.

טכניקות לסימולציה של גרעיני ננו־הלום טבולים בפחמן אמורפי פותחו לצורך סימולציות מדויקות של ננו־הלומים. סוג חדש של מודל, ה-mixed sample, פותח לצורך ביצוע סימולציות של תופעות חדשות, כגון גידול של ננו־הלומים על-ידי Chemical Vapor Deposition שנעשה בטכניון. שיטות חישוביות לחקר סוג זה של מודל פותחו גם כן.

טכניקות ויזואליזציה באמצעות תוכנת AViz שופרו. כלי־עזר פותחו לצורך הפקת התוצאות המיטביות מהתוכנה. טכניקות אלה שימשו למחקרים נוספים בקבוצה. מהתוצאות בולט הקשר בין חישוב מצבי אנרגיה שנעשה באמצעות Tight Binding



והתוצאות הניסיוניות של NEXAFS. בנוסף, תוצאות מהתפלגויות רדיאליות וזוויתיות שחושבו על הדגמים והאפיון של מצבי היברידיזציה מחזקים את הנכונות של תהליך בניית הדגמים האמורפיים והמעורבים. תוצאות חישוביות של דגמים מעורבים בהשוואה למדידות ניסיוניות מצדיקות את התיאור של הדגמים הניסיוניים כליבות של ננו-יהלומים בתוך מטריצה אמורפית.

בהשוואת חישובים של צפיפות מצבים כנגד מדידות של NEXAFS ניתן לראות שכל המאפיינים העיקריים שלהם משותפים ובעלי מתאם איכותי. לכן, אנו יכולים לומר בבטחה שהקשר שהונח בין חישובי צפיפות המצבים ב-Tight Binding molecular dynamics ומדידות NEXAFS אכן תקף. צעדים התחלתיים בסימולציה של מודלים בתוספת אטומי מימן בוצעו בהצלחה.